Thermodynamic Bounds of Terrestrial Water-Energy Coupling and Resiliency in Global Ecosystems

Debasish Mishra[1], Vinit Sehgal[1,2,3], and Binayak P Mohanty[1]

[1]Biological and Agricultural Engineering, Texas A&M University
[2]Water Management and Hydrological Science, Texas A&M University
[3]School of Plant, Environment, and Soil Sciences, Louisiana State University

November 20, 2023

Abstract

Increasing climatic variability has resulted in an unprecedented surge in extreme events, pressing global ecosystems towards systematic breakdown. Yet, the resilience of the soil-vegetation-atmosphere (SVA) system to revert to its natural state indicates the existence of energetic barriers forbidding systems from tipping. Observational and theoretical constraints limit our understanding of these energetic barriers which are crucial for assessing ecosystem sensitivity to atmospheric perturbations. We provide a novel coherent theory on the dissipative energy barriers (?e) which decides the resilience potential of an ecosystem. These barriers are manifestation of lower bounds of entropy produced (Σ *) for unit anomaly transference from soil moisture (SM) to evapotranspiration (ET). Using remote sensing data, we compute these global entropy bounds by introducing a new metric (Wasserstein distance, dw) for SM-ET coupling. Quantifying these lower bounds from SM-ET coupling, places terrestrial ecosystems in the hierarchy of dissipative energy states spanning from forested regions to barren lands. Furthermore, we show that the optimization of SM-ET coupling translates to entanglement of water potential gradient ([?]ω) between land surface and atmospheric boundary layer, and the resulting memory timescale or residence time (τ). This (τ.[?]o) entanglement propels moisture-rich and moisture-deficit systems in complementary evolutionary pathways in responding to imposed anomalies. As a result, we witness an emergence of coupling-aridity tradeoff with temperate climates operating as least efficient systems for unit SM to ET anomaly transfer. Physical basis, and transferability across space and scale makes this theory a potential benchmark for process improvement in the climate and earth system models.

Thermodynamic Bounds of Terrestrial Water-Energy Coupling and Resiliency in Global Ecosystems

Debasish Mishra[1], Vinit Sehgal[1,2,3], Binayak P. Mohanty[1]*

[1]Biological and Agricultural Engineering, Texas A&M University, TX 77843, USA
[2]Water Management and Hydrological Science, Texas A&M University, TX 77843, USA
[3] Now at the School of Plant, Environment, and Soil Sciences, Louisiana State University, LA 70801, USA

*Corresponding author: Binayak P. Mohanty (bmohanty@tamu.edu)

Submitted to

Water Resources Research

Submitted on November 12th, 2023

Key Points:

- Lower entropy bounds and evolutionary pathways were quantified for unit SM-ET anomaly transference.
- Existence of SM-ET coupling-aridity tradeoff was observed with temperate climates representing least efficient systems.
- Terrestrial ecosystems arrange in a hierarchical order of entropic thresholds with forested ecosystems occupying top of the hierarchy.

Keywords: Water - Energy Coupling, Entropy Bounds, Optimal Transport, Water Potential Gradient, Memory Time Scale, Dissipative Energy Barrier

Abstract

Increasing climatic variability has resulted in an unprecedented surge in extreme events, pressing global ecosystems towards systematic breakdown. Yet, the resilience of the soil-vegetation-atmosphere (SVA) system to revert to its natural state indicates the existence of energetic barriers forbidding systems from tipping. Observational and theoretical constraints limit our understanding of these energetic barriers which are crucial for assessing ecosystem sensitivity to atmospheric perturbations. We provide a novel coherent theory on the dissipative energy barriers (Δe) which decides the resilience potential of an ecosystem. These barriers are manifestation of lower bounds of entropy produced (Σ^*) for unit anomaly transference from soil moisture (SM) to evapotranspiration (ET). Using remote sensing data, we compute these global entropy bounds by introducing a new metric (Wasserstein distance, d_W) for SM-ET coupling. Quantifying these lower bounds from SM-ET coupling, places terrestrial ecosystems in the hierarchy of dissipative energy states spanning from forested regions to barren lands. Furthermore, we show that the optimization of SM-ET coupling translates to entanglement of water potential gradient ($\Delta\omega$) between land surface and atmospheric boundary layer, and the resulting memory timescale or residence time (τ). This ($\tau.\Delta\omega$) entanglement propels moisture-rich and moisture-deficit systems in complementary evolutionary pathways in responding to imposed anomalies. As a result, we witness an emergence of coupling-aridity tradeoff with temperate climates operating as least efficient systems for unit SM to ET anomaly transfer. Physical basis, and transferability across space and scale makes this theory a potential benchmark for process improvement in the climate and earth system models.

Plain Language Summary

In recent years, extreme events have put a lot of pressure on the planet's ecosystems, but they seem to have a natural ability to bounce back. However, a fully developed mechanical understanding of these energy barriers that stop these systems from tipping is lacking. We argue that the effects of atmospheric disturbances on land surfaces can be comprehended from their interaction through signatures in soil moisture (SM) – evapotranspiration (ET) coupling. Hence, quantifying the entropy thresholds for unit anomaly transfer from SM to ET can provide new means for computing the resilience of ecosystems. Using an optimization framework, it is shown that the driving water potential ($\Delta\omega$) and memory timescale (τ) of moisture anomalies are entangled. This has repercussions on how global hydroclimates cope up with varied level of atmospheric dryness. This theory could be a useful tool for improving climate and Earth system models because it's based on physical principles and can be applied to different places and scales.

I. Introduction

Recent years have witnessed a surge in weather-related extremes across the globe, boosting the "dry getting dryer, and wet getting wetter" paradigm over the majority of terrestrial landscapes (Dosio et al., 2018; Perkins-Kirkpatrick & Lewis, 2020). Comprehending the land surface responses to these atmospheric perturbations has thus become of increasing significance, for improving climate forecasts and predicting ecosystem resilience (Sehgal et al., 2021; Verbesselt et al., 2016). The coupled terrestrial water-energy system entails signatures from these continuous atmospheric perturbations, the imprints of which are registered in soil-vegetation response through changes in soil moisture (SM) - evapotranspiration (ET) coupling (Dirmeyer, 2011; Koster et al., 2004; Seneviratne et al., 2006). Intricately connected to SM-ET coupling is the concept of memory timescale (τ), defined as the time needed by a land unit to forget an imposed anomaly (Koster & Suarez, 2001; McColl et al., 2017). Conventionally, τ has been quantified using the autocorrelation of SM time series with previous literature observing similar timescales under spatially distinct regions of the world (Ghannam et al., 2016; McColl et al., 2019; Teuling et al., 2006). Given the importance τ plays in modulating land-atmospheric feedback, such overlapping results provokes a deeper question of whether a unifying governing principle underlies these empirically observed timescales, and if so, to what extent does the presence of such a principle impact the dynamics of terrestrial water-energy interactions?

As soil moisture evaporation (and transpiration through plants) involves irreversible heat and mass transfer, thermodynamics serves as a universal means to declutter SM-ET coupling dynamism from an energy perspective. A continuous atmospheric circulation maintains water potential gradient and results in sustained entropy production through SM-ET conversion (Kleidon, 2008). The presence of water potential gradient also signifies non-equilibrium (NE) state, and the maximum entropy production (MEP) principle states that system in NE will adapt to *steady states* at which they dissipate energy and produce entropy at the maximum possible rate (Kleidon, 2010). Under such conditions, the rate of change in SM and ET approaches a nearly constant value inherent to the system (Kleidon, 2010), defined here as *non-equilibrium steady state* (NESS), and characterized by nonzero fluxes and nonzero potential gradients (Qian, 2006). Hence, entropy production quantifies how much a physical system is driven away from equilibrium by capturing a system's evolution (in this case SM-ET coupling) in response to the environment.

From a systems perspective, a hydroclimate can be thought of as a particular configuration of soil-vegetation-atmosphere (SVA) characterized by long-term *expected* behavior in process interactions constrained upon energy fluxes in and out of the system. Responses of SVA systems to changes in atmospheric forcings are dependent on the nonlinear relationship between energy fluxes and soil moisture (Feldman et al., 2022). Nevertheless, when supported by soil hydrological processes (SHP) in modulating the impact of atmospheric perturbations, hydroclimates across the globe often demonstrate the tendency to return back pre-anomaly conditions - described as *resilience* of the system in previous literatures (Berdugo et al., 2020; Fu et al., 2022; Verbesselt et al., 2016). This is evident from responses displayed by most systems to frequent and seasonal atmospheric perturbations within meteorological (and often climatic) time scales through gradual recovery to optimum NESS. Hence, resilience can be considered the tendency of SVA to *hold-on* to NESS, unique to a SVA configuration. We hypothesize that the resilience of any SVA to maintain its configuration in a preferred NESS is compensated by paying through equivalent entropy production. Hence, any change in SVA will be induced through changes in entropy production and preferred NESS.

However, with changing climate, the modulating capacity of SHP are severely impacted (Seneviratne et al., 2006; Vereecken et al., 2022) rendering a higher probability for the system's threshold to be crossed and making the system vulnerable to topple into a new stable state with different NESS (Berdugo et al., 2020). Therefore, it becomes critical to quantify these lower bounds of the entropy barrier which when crossed will alter the climate to a new stable state defining transitions between hydroclimates. Statistical physics literature has delved into the explainability of optimal control of stochastic thermodynamic systems using optimal transport (OT) theory (Benamou & Brenier, 2000; Dechant, 2022; Dechant & Sakurai, 2019; Nakazato &

Ito, 2021; Van Vu & Saito, 2022). OT concerns the means by which one can optimally transport a source distribution to a target distribution, characterized by a metric called the Wasserstein distance (d_W) (Dechant & Sakurai, 2019; Van Vu & Saito, 2022). Studies have shown that for a stochastic process, the lower bound of entropy production could be expressed as a function of d_W between the initial and final states of the system's distribution (Dechant, 2022). We adapt d_W as the coupling metric and derive the expression for lower bound of entropy production in SM-ET transitioning, with water moving from soil to atmosphere or soil to plant to atmosphere. Furthermore, using equivalence between statistical and classical thermodynamics, we show that the optimization of SM-ET coupling transcends to the entanglement of the water potential gradient ($\Delta\omega$) which drives the moisture out of the system and the resulting memory timescale (τ), or residence time across root water uptake to stomatal expulsion.

In this study, we aim to answer a key question: When there's an exchange of anomalies from soil moisture (SM) to evapotranspiration (ET), what is the minimum memory timescale and entropy production required for this process? To achieve this, the paper addresses three primary objectives: (1) determine the minimum levels of entropy production needed for various global hydroclimates for unit anomaly transference, (2) establish a fundamental relationship between the strength of the coupling between SM and ET and the memory timescale, and (3) investigate the evolutionary paths taken by climatic systems that adhere to these proposed optimization principles. Additionally, we develop a coherent theory concerning the resilience of ecosystems by introducing the concept of dissipative energy barriers (DEB), which are derived from entropic thresholds at which a system operates.

2. Data Set

2.1 Satellite SM and ET Datasets

Combined (active + passive) surface soil moisture (SSM) data (Lopez, 2018) provided by Copernicus Climate Change Service (C3S) for the period Jan 2010 – Dec 2019 was used for the analysis. The product is gridded at 0.25° x 0.25° spatial and 1 day temporal resolution, and captures the top few centimeters of the soil where the land-atmosphere mass exchanges and biological processes for plant growth are concentrated (Ouedraogo et al., 2013). Supplementary Table S1 outlines the sensors used for producing the combined product. Recent studies have shown that surface moisture carries information about deeper profiles beyond the generally attested top 5cm (Short Gianotti et al., 2019) and can inform about evapotranspiration regime changes (Dong et al., 2022). To avoid ambiguity, we will denote surface moisture as SM.

For evapotranspiration (ET), the gap-filled product from Terra MODIS (i.e., MOD16A2GF) for the period 2010-2019 was used for the analysis (Running et al., 2019). It is based on the Penman-Monteith equation and is available at 500 m spatial resolution and temporally as 8-day composite i.e., pixel values are the sum of all eight days within the composite period.

2.2 Ancillary Datasets

Water - Energy clustering (WEC) classification proposed by Pisarello & Jawitz (2021) were used for global hydroclimate reference owing to its inclusion of ET into the classification scheme. The 15 WEC zones were resampled into five primary groups based on increasing zone mean aridity index (φ = Potential Evapotranspiration (PET)/Precipitation (P)), namely Super Humid ($\varphi = 0.39$), Humid ($\varphi = 0.58$), Temperate ($\varphi = 1.07$), Arid ($\varphi = 2.05$), and Hyper Arid ($\varphi = 9.56$). MODIS Annual International Geosphere-Biosphere Program (IGBP) classification (Sulla-Menashe et al., 2019) was used for ecosystem classification. We broadly categorize them into forests (F), savannahs (SV), croplands (CRP), grasslands (GR), shrublands (SH), and barren land (B). Bias corrected ERA5 reanalysis meteorological and soil temperature datasets (supplementary

Table S2) were used for computation for near surface boundary layer chemical water potential and entropy production. van Genuchten soil water characteristics (SWC) and saturated hydraulic conductivity parameters provided in (Gupta et al., 2020, 2022) were used along with vegetation hydraulic parameters provided in Liu et al. (2021) for soil and vegetation matric potential calculation, respectively. MODIS NDVI (Didan, 2015) data was used for vegetation water content calculation. Canopy height derived from sentinel-2 images (Lang et al., 2022) were used as proxy for travel length for water particles.

All datasets were linearly rescaled to 0.25° x 0.25° spatial resolution (hereon referred as *footprint* scale) through bilinear interpolation and spaced at 8-day temporal resolution in accordance with MODIS ET retrieval dates. Ancillary datasets were spatially resampled to match the extents of SM and ET raster's and averaged over four seasons (MAM - March through May, JJA - June through July, SON - September through November, DJF - December through February). Data processing and analyses were done in the R environment (RStudio 2022.12.0+353), and optimal transport calculations were performed using the transport library (Schuhmacher et al., 2022).

3. Methodology

3.1 Unit anomaly transference and Non-Equilibrium Steady State (NESS)

A variety of micro-scale mechanisms govern flow transport and SM-ET coupling, and describing their footprint scale manifestation requires generalization of the representative dominant processes (also termed as "*effective"* processes) keeping the pore-scale physical description intact (Blöschl & Sivapalan, 1995; Crow et al., 2012; Mohanty, 2013; H. Vereecken et al., 2007). Utilizing the fundamental mass balance and phase change kinetics, Ouedraogo et al., (2013) described a non-equilibrium model for water transport (equation 1 and 2),

$$\frac{\partial \rho_l}{\partial t} + \nabla.(\rho_l\, v_l) = -\widehat{\rho_v} \quad (1)$$

$$\frac{\partial \rho_v}{\partial t} + \nabla.(J_v) = \widehat{\rho_v} \quad (2)$$

where ρ_l and ρ_v (kg m^{-3}) are the apparent density of soil water and its vapor respectively, v_l (m s^{-1}) is the soil water flux, J_v (kg m^{-2} s^{-1}) is the vapor diffusion flux, and $\widehat{\rho_v}$ (kg m^{-3} s^{-1}) is the phase-change rate. Assuming a strong degree of coordination between liquid and vapor phase water transport (Katul et al., 2012), the soil-plant hydrodynamics for vertical water motion on a footprint scale, equation (1) and (2) can be combined to form a generalized continuity equation described in terms of effective diffusion flux,

$$\frac{\partial \rho_{eff}}{\partial t} + \nabla.\left(J_{eff}\right) = 0 \quad (3)$$

where ρ_{eff} (= ρ_l + ρ_v) is the effective density of liquid water and vapor, and J_{eff} (= $\rho_l\, v_l$ + J_v) is the effective diffusion flux resulting from effective velocity field $v_{eff}(x)$ which is a function of both time t and position x of the particle undergoing diffusion. Here, effective velocity describes the net directional movement of water molecules with which they are transported through soil-vegetation continuum during ET. Many experimental studies on evaporation in porous media have suggested the dominance of vapor flow near the surface (~ 20 to 100 mm) (Brutsaert, 2014; Lehmann et al., 2008; Shokri et al., 2009). As such for footprint observations of surface retrievals, we assume SM-ET anomaly transference (water transport) to be dominated by diffusive fluxes and an instantaneous phase change. The rate of change of these transport fluxes can be described in terms of NESS, defined as the section of the dynamic regime where SVA spends most of its time, and mathematically represented as the mode of the distribution,

$$NESS_X = \lim_{\Delta\left(\frac{X_{t_j} - X_{t_i}}{t_j - t_i}\right) \to c} \frac{X_{t_j} - X_{t_i}}{t_j - t_i} \quad (4)$$

where X_{t_i} and X_{t_j} are successive observations at time t_i and t_j. Here the limit reflects the slowing down in rate of change to a steadier value *c* in the neighborhood of 0 – function of soil and vegetation type. Thus, NESS represents the coherent macroscopic ensemble of the SM and ET at footprint scale. For application of OT, $NESS_{SM}$ and $NESS_{ET}$ are expressed in the same configuration space using a dimensionless quantity called the Anomaly Impact Factor (AIF), defined as the ratio of rate of change of variable at incremental time steps divided by its long-term standard deviation σ,

$$AIF_X = \frac{\left(\frac{x_{t_j} - x_{t_i}}{t_j - t_i}\right)}{\sigma_{\left(\frac{x_{t_j} - x_{t_i}}{t_j - t_i}\right)}} \quad (5)$$

AIF configuration space (Fig. 1) displays the transformation of SM anomalies distribution to ET anomalies distribution through an OT framework and provides an advantage of envisioning SM-ET coupling from a disturbance propagation point of view.

3.2 Optimal Transport Framework for SM-ET coupling

Evolution, when stated in terms of statistical physics, is probable motion (Kaila & Annila, 2008). OT provides a linkage between time evolution of probability density of a diffusing particle and associated entropy production through an analogy to least work done (energy optimum) by the system. We consider the distance cost function *c(x,y)* of transporting a single water particle at the point x ∈ SM_{AIF} to the point y ∈ ET_{AIF}, both defined on AIF configuration space (Fig. 1). Our aim is to minimize *c(x,y)* subject to all possible paths of transferring the particle from SM_{AIF} distribution (say *s(x)*) to ET_{AIF} distribution (say *e(y)*). According to Monge-Kantrovich (MG) minimization problem, the optimal transport cost for *c(x,y)* between two probability distributions *s(x)* and *e(y)* is defined as

$$C(s,e) = \min_{\pi \epsilon \delta(s,e)} \int c(x,y)\pi(x,y)dxdy \quad (6)$$

where the lower bound is taken over the entire set $\delta(s,e)$ of joint probability distributions $\pi(x,y)$ whose marginal distributions are $s(x)$ and $e(y)$, i.e,

$$\delta(s,e) = \begin{Bmatrix} \pi | s(x) = \int \pi(x,y)dy, \\ e(y) = \int \pi(x,y)dx \end{Bmatrix} \qquad (7)$$

s.t. $\pi(x,y) \geq 0$

Hence, the optimal transport cost gives a minimum of the expected value of the cost $c(x,y)$ for the joint distribution $\pi(x,y)$, also referred to as the optimal transport plan (Nakazato & Ito, 2021). Considering L^2 norm as the optimal transport cost on the AIF space leads to the L^2 - d_W. Explicitly, the L^2 - d_W between s and e is defined as

$$d_W(s,e)^2 = \min_{\pi \epsilon \omega(s,e)} \int ||x-y||^2 \pi(x,y)dxdy \qquad (8)$$

which is equivalent to optimal transport cost $C(s,e)$ for the cost function $c(x,y) = ||x - y||^2$. Thus, d_W as an optimal coupling measure quantifies the Euclidean length-scale for transferring a unit anomaly from SM_{AIF} to ET_{AIF}. A low d_W indicates immediate coupling, while a larger d_W indicates delayed coupling (Fig 1). Here on, d_W will mean L^2 - d_W and $d_W(s,e)^2$ will be represented as ${d_W}^2$ in short.

3.3 A Comprehensive SM-ET coupling framework

Owing to the critical role played by SM-ET coupling, the topic has received a lot of attention over the years with studies often suggesting contrasting results for similar regions (Koster et al., 2004; Seneviratne et al., 2010; Tuttle & Salvucci, 2016). The discrepancies in previous coupling studies stems primarily from the methodology applied (modeled versus observation based) and corresponding perception of terminologies (positive versus negative coupling, strong versus weak coupling). Here we propose a more comprehensive division of SM-ET coupling (Fig. 1) starting with a broader segmentation into (a) *instant (or immediate) coupling* ($d_W < 1$), and (b) *delayed (or deferred) coupling* ($d_W > 1$). The instant coupled systems are further branched into (a) *dry-coupled* (AIF < 0), and (b) *wet-coupled* (AIF > 0) systems. Dry-coupled systems are regions which preferentially stay in dry regime (and SM limited) for both SM and ET (for example, arid and hyper arid regions). These dry-coupled systems are predominantly demand-driven, i.e., a high vapor pressure deficit allows for quicker transference of anomalies referred to as pulse reserve mechanism in previous literature (Feldman et al., 2018). On the other extreme are wet-coupled systems demarcating regions with wet regime preferences (for example humid and super humid regions). These systems are primarily supply-driven, i.e., a relatively higher SM replenishment maintains continuous infusion of moisture into the atmosphere. These systems have higher moist static energy (Eltahir, 1998).

In between the dry-coupled and wet-coupled systems, temperate regions may be featured, which are largely governed by delayed coupling. However, based on the lagging distribution limb these delays could be further classified into (i) *dry-delay*, and (ii) *wet-delay*. The regions where surface SM drying (or wetting) does not produce quicker imprints on ET, fall under the purview of dry (or wet) delayed systems. These can be inferred from spatial maps of fraction of time a pixel spends in dry or wet regime at any given season. The advantage of such a division is that it naturally advances the widely accepted ideas of preferential states of soil moisture (D'Odorico & Porporato, 2004; Grayson et al., 1997; Sehgal & Mohanty, 2023) and Budyko framework (Budyko, 1974), while forgoing earlier terminology conflicts. Additionally, the division allows for quantification of SM-ET coupling using d_W which has extensions to understand corresponding entropy production (described in section 3.4) in SM to ET anomaly transference. It is to be noted that the proposed division leverages on the fact that vertical forces are dominant over lateral forces and gravity drainage is seldom captured at footprint scale (Sehgal et al., 2021), hence, all SM anomalies retrieved are registered as ET anomalies. This simplification provides flexibility in application of mass continuity equation (and thus *pdf* conservation).

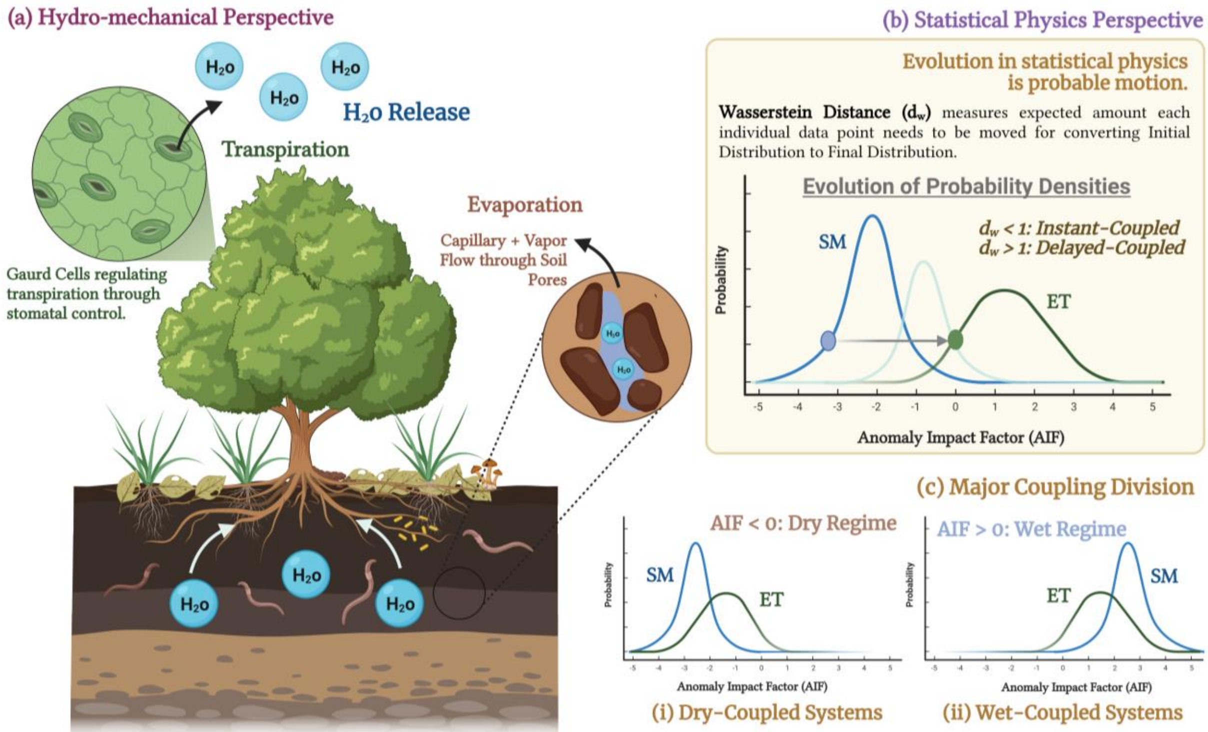

Figure 1. Schematic describing the proposed SM-ET coupling from (a) hydro-mechanical perspective to corresponding (b) statistical physics perspective condensed in the form of SM (blue) and ET (green) anomaly impact factor (AIF) distributions. Grey arrow from a single $\mathrm{SM}_{\mathrm{AIF}}$ (blue circle) to most likely $\mathrm{ET}_{\mathrm{AIF}}$ (green circle) represents transport instance satisfying optimal cost function. Wasserstein distance (d_W) is the mean value of the square of optimal transportation distance represented by the length of the arrows connecting all perturbation points from $\mathrm{SM}_{\mathrm{AIF}}$ to $\mathrm{ET}_{\mathrm{AIF}}$. (c) Based on Anomaly Impact Factor (AIF) values, global SM-ET coupling schemes are divided broadly into dry coupled (AIF < 0) and wet-coupled (AIF > 0) systems. These can be further divided into immediate coupling represented by closely spaced AIF distributions with $d_W < 1$, and delayed coupling represented by distanced AIF distributions with high $d_W > 1$.

3.4 Lower bound of Entropy production and Wasserstein Distance relationship

Due to the open-system attributes of the land surface, both heat and mass flow across its boundaries producing entropy, with the transport of latent heat by vapor flux being the significant coupling process (Ouedraogo et al., 2013). Benamou & Brenier (2000) were able to prove that for a particle obeying diffusion equation of the form expressed in equation 3, the d_W bears direct linkage to continuum mechanics formulation that states: (1) d_W gives the lower bound on the expected value of the square of the effective velocity field $v_{eff}(x)$,

$$d_W{}^2 \leq \tau \int_0^\tau \int \left|\left|v_{eff}(x)\right|\right|^2 p_t(x)dxdt \tag{9}$$

where $p_t(x)$ is the probability density of the particle's position at any time t, and (2) the local mean velocity can be related to entropy production as

$$\Sigma_t = \frac{1}{\mu T} \int ||v_{eff}(x)||^2 p_t(x)dx \tag{10}$$

where we consider the time integral from time t = 0 to time t = τ. Comparing equations (9) and (10), the minimum entropy production associated with changing the probability density from an initial state s (in SM) to a final state e (in ET) can be expressed in terms of d_W,

$$\Sigma_t \geq \frac{1}{\mu\, T_{surf}\, \tau} d_W(s,e)^2 \tag{11}$$

where τ (s) is the duration of the anomaly transfer process or memory timescale, μ (s kg^{-1}) is water particle mobility, T_{surf} (K) is temperature of the land (soil + vegetation) surface, and Σ_t (J m^{-2} K^{-1}) is the entropy produced. Hence, for a stochastic process connecting the initial and final states, the right-hand side of equation 11 gives the lower bound on the entropy production, say Σ^*. An important consequence of equation 11 is the existence of a unique thermodynamic force which realizes minimal dissipation (Dechant & Sakurai, 2019).

Kinetic theory of gases defines mobility (μ) of a particle as the ratio of drift velocity and force field. From an analogous treatment, we consider the directional movement of water molecules as the "effective" velocity with which they are transported in the SVA continuum under an applied force field. So, the water particle mobility can be written as:

$$\mu = \frac{v_{eff}}{F_{eff}} \tag{12}$$

From Newton's second law:

$$F_{eff} = \frac{d(mv_{eff})}{dt} = m \times \left(\frac{dv_{eff}}{dt}\right) + v_{eff} \times \left(\frac{dm}{dt}\right) \tag{13}$$

The rate of change in effective velocity (*first term*) is order of magnitudes smaller than mass flux contribution (*second term*), and hence can be neglected, giving a first order approximation of equation (13):

$$F_{eff} \equiv v_{eff} \times \left(\frac{dm}{dt}\right) \tag{14}$$

This mass flux on a footprint scale is the amount of water vapor leaving the surface, i.e., physically equivalent to ET (kg s^{-1}),

$$F_{eff} \equiv v_{eff} \times \mathrm{ET} \tag{15}$$

From equation (12) and (15) we obtain

$$\mu = \frac{1}{ET} \tag{16}$$

Here we note that the mass flux leaving the surface is dependent on external parameters such as temperature, vapor gradient, partitioning of net radiation, roughness of land surface, etc. but following the argument by (Brutsaert, 2014) that the moment-to-moment changes of these additional factors compensate each other, these are omitted for brevity. Hence, on a footprint scale, this force and resulting field enables the effective water particle mobility which can be equivalently expressed as the inverse of ET expressed in kg s^{-1} (supplementary material),

$$\Sigma^* = \frac{ET}{T_{surf}\,\tau} d_W(s,e)^2 \tag{17}$$

3.5 Optimization entanglement and the physical significance of Wasserstein Distance

Using classical formulations, earlier literatures (Kleidon, 2008; Porada et al., 2011) proposed entropy production for ET to be function of chemical potential gradient ($\Delta\omega$) between atmospheric boundary layer and diffusing surface:

$$\Sigma = \frac{ET}{T_{surf}} \Delta\omega \tag{18}$$

The diffusing surface, here, denotes the surface from where water particle escapes to the atmosphere, for example, soil surface for a barren open land or leaf surface for a vegetated area. The chemical potential of water is defined as the free energy per mole of water and elaborates the potential for a substance to move, or in other words, to do work. The statistical formulation (Eqn. 17) and classical formulation (Eqn. 18) are analogues in construction. By introducing a constant of proportionality, we can equate both the formulations to obtain:

$$d_W(s,e)^2 = \mathscr{k}.\tau.\Delta\omega \tag{19}$$

where $\mathscr{k}$ is proportionality constant (expressed in kg/J-s) which establishes a connection between the statistical and classical formulation. The product ($\tau.\Delta\omega$) in eqn. (14) is equivalent to *action* (per unit mass) in classical mechanics which describes how a physical system evolves over time. Mathematically, action is a functional which takes the trajectory of the system as its argument and integrated over time span of state evolution. Hence, it is path dependent and the principle of least action (Sussman & Wisdom, 2001) postulates that the path followed by a physical system is that for which the action is minimized. In the context of SM-ET coupling, it means that the water particle will always follow the path that minimizes the time-averaged $\Delta\omega$. Therefore, τ and $\Delta\omega$ are entangled such that the product $(\tau.\Delta\omega)$ will always be optimized. As such, the optimization of d_W from MG minimization problem can be rooted in terms of classical treatment as the optimization (minimization) of entangled space of values for $(\tau.\Delta\omega)$. Thus, d_W as the Euclidean length-scale can be defined as the path equivalent that optimizes $(\tau.\Delta\omega)$ for a unit water potential gradient. In other words, optimization of SM-ET coupling leads to $(\tau.\Delta\omega)$ entanglement giving the lower bound on the entropy production as the action measured by the path length of the d_W (Nakazato & Ito, 2021).

3.6 Memory timescale formulation

By virtue of this entanglement, the optimization formulation yields:

$$\frac{\partial(\tau.\Delta\omega)}{\partial {d_W}^2} = 0 \quad (20)$$

Expanding by chain rule, we obtain:

$$\Delta\omega \times \frac{\partial(\tau)}{\partial {d_W}^2} + \tau \times \frac{\partial(\Delta\omega)}{\partial {d_W}^2} = 0 \quad (21)$$

$$\Delta\omega \times \frac{\partial(\tau)}{\partial {d_W}^2} + \tau \times \frac{1}{\gamma} = 0 \quad (22)$$

where γ is the seasonal slope of ${d_W}^2$versus $\Delta\omega$ plot and describes the sensitivity of SM-ET coupling to the induced potential gradients. Dividing (22) by $\Delta\omega$, we obtain:

$$\frac{\partial(\tau)}{\partial {d_W}^2} + \frac{1}{\gamma\Delta\omega} \times \tau = 0 \quad (23)$$

Equation (23) represents a first order homogeneous differential equation whose solution is:

$$\tau = \tau_0 \exp\left(\frac{-{d_W}^2}{\gamma\Delta\omega}\right) \quad (24)$$

where τ_0 is the integral constant, hereon defined as the inherent timescale of anomaly transference. The dimensionless quantity (τ/τ_0) can be used as a fundamental descriptor of water-energy coupling for a hydroclimate under induced potential gradients. To keep the problem tractable, we will consider a rudimentary approximation of $\tau_0 = L_d/K_{eff}$, where L_d is the traverse length for water particle, and K_{eff} is the effective conductivity of the land surface. We acknowledge that the solution for eqn. (24) is dependent on the initial value τ_0 whose approximation using rudimentary approach may not be appropriate for all cases but nevertheless, it provides a first order estimation of τ for testing our hypothesis and comparing it with results from earlier literatures.

3.7 Chemical potential gradient as thermodynamic force

To understand the functional form of the optimization entanglement, we compute chemical potential gradient ($\Delta\omega$) which is the absolute difference between atmospheric boundary layer potential and diffusing surface potential:

$$\Delta\omega = \left|\omega_{bl} - \omega_{surf}\right| \tag{25}$$

where $\omega_{surf} = \left(\omega_{soil} + \omega_{veg}\right)$ is the diffusing surface potential. The potential of water vapor in the atmospheric boundary layer is computed as:

$$\omega_{bl} = R_{vap}T_{air}ln(RH) + gz_{air} \tag{26}$$

where R_{vap} is the specific gas constant of water vapor (= 461.5J kg^{-1} K^{-1}), T_{air} and *RH* are the mean temperature and relative humidity of the boundary layer, respectively, g is the acceleration due to gravity, and z_{air} is the height of measurement relative to mean sea level. Pixels with *RH* > 1 (*super saturated condition*) were removed from the analysis. The water potential in the vegetation is computed using:

$$\omega_{veg} = \left(\theta_{veg} - 1.0\right) \times \Psi_{PWP} \tag{27}$$

θ_{veg} is the relative vegetation water content and Ψ_{PWP} is the permanent wilting point which is set to an upper threshold of 1471.5 J kg^{-1} (Porada et al., 2011). The vegetation water content (in *kg m^{-2}*) was derived from normalized difference vegetation index (NDVI) data using SMAP algorithm (Chan, 2013):

$$\theta^*_{veg} = (1.9134 \times NDVI^2 - 0.3215 \times NDVI) + stem\ factor \times \left(\frac{NDVI_{max} - NDVI_{min}}{1 - NDVI_{min}}\right) \tag{28}$$

The soil water potential is a sum of matric (Ψ_m) and gravitational (gz_{surf}) potential.

$$\omega_{soil} = \Psi_m + gz_{surf} \tag{29}$$

where z_{surf} is the depth of water table from soil surface. Because we are concerned with the difference in potential $\Delta\omega$, the difference in gravitational potential $(z_{air} - z_{surf})g$ is taken an average value of $2 \times g$ as the values of reanalysis meteorological variables are quantified for a height of 2m above the land surface. For Ψ_m, we used van Genuchten (vG) soil water retention curve (SWC) (van Genuchten, 1980) for computation,

$$S_{eff} = \frac{\theta - \theta_r}{\theta_s - \theta_r} = \frac{1}{[1 + (\alpha|\Psi_m|^n)]^{1-1/n}} \tag{30}$$

where S_{eff}(-) is the effective saturation, θ (m^3 m^{-3}) is the soil moisture reading, θ_s (m^3 m^{-3}) is saturated water content, θ_r (m^3 m^{-3}) is residual water content, α (m^{-1}) is inverse of the air entry pressure, n (-) is measure of the pore-size distribution, and Ψ (m) is the soil matric potential. Gupta et al. (2022 and 2020) provide maps of global vG parameters values (α, n, θ_r and θ_s) and saturated hydraulic conductivity (K_s) at field scale (i.e., 1 km spatial resolution). For converting these field-scale parameters to footprint scale effective values, we employ the upscaling guidelines set by Zhu & Mohanty (2002) for heterogeneous soils with variable saturation: arithmetic means for K_s and n, a value between arithmetic and geometric means for α when K_s and α are highly correlated, and a value between geometric and harmonic means for α when K_s and α are poorly correlated. Note that correlation here refers to the parameter correlation of the coherency spectrum. For computation of τ_0, L_d was approximated to canopy height + top soil depth (= 0.05m), while effective hydraulic conductivity was computed using series formulation, i.e., $K_{eff} = (K_{plant} \times K_{soil})/(K_{plant} + K_{soil})$ for vegetated surface and = K_{soil} for barren lands, expressed in m/s. Note that to reduce the artificial speckling effect introduced due to piecewise regression for computing γ, we smooth out the resulting raster for τ using a focal aggregation of 7x7 window.

4. Results and Discussion

4.1 Global Non - Equilibrium Steady States of SM ($NESS_{SM}$) and ET ($NESS_{ET}$)

Fig. 2 and 3 showcase the seasonal variation in $NESS_{SM}$ and $NESS_{ET}$ globally. The non-equilibrium situation is caused by replacing the partially saturated air with relatively drier air parcels by continuous atmospheric circulation which results in a macroscopic thermodynamic non-equilibrium between SM and ET. Soil drying (negative $NESS_{SM}$) is dominantly prevalent across landscapes except when atmospheric forcings such as precipitation or melting of snow causes soil to predominantly wet. Whereas the spatial structuring for $NESS_{ET}$ reflects seasonally dominant - latitudinal patterns with southward successive shifts in positive $NESS_{ET}$, starting from northern-mid latitudes in MAM, to northern-tropical latitudes in JJA and to southern counterparts during SON and DJF seasons.

During MAM, wet anomaly (positive $NESS_{SM}$) is prevalent at higher latitudes, Sahel region of Africa, eastern Asia (Central and Northeastern China, North Korea, Laos, Cambodia, Thailand, and Vietnam), and parts of southern Australia. During JJA, the monsoonal rainfall in Sahel region, Indian subcontinent and the western Mexico intensifies the wetting of soil (Fig. 2). The dual availability of moisture and energy allows the monsoonal imprints observed in $NESS_{SM}$

to be transferred to $NESS_{ET}$ with increasing flux rates throughout JJA (Fig 3). However, these regions undergo a complete reversal in the following seasons of SON and DJF.

Global arid and hyper-arid regions (western CONUS, Iberian Peninsula, central west Australia, southern Africa, and southern east South America) display a declining flux rate throughout all seasons. Interestingly, most of the CONUS spends more time drying soil than wetting except evergreen forest in northwestern coastline in SON (Fig. 2). One important attribute in case of Australian climate is the central deserted region which across all seasons remain in the desiccated state or nearly zero $NESS_{SM}$ which is a physical manifestation of low moisture leading to lower capacity to lose moisture further. The insets in Fig. 2 and 3 represent variations of $NESS_{SM}$ and $NESS_{ET}$ observed across hydroclimates. These insets highlight two unique features about seasonal climatic distribution (i) compared to $NESS_{SM}$, a higher *in-class* variance is observed in $NESS_{ET}$, a characteristic most likely attributed to atmospheric fluctuations, and (ii) across classes, the seasonal variability is higher in temperate climates followed by humid regions, while super humid and hyper arid regions display relatively stable cross-season distribution.

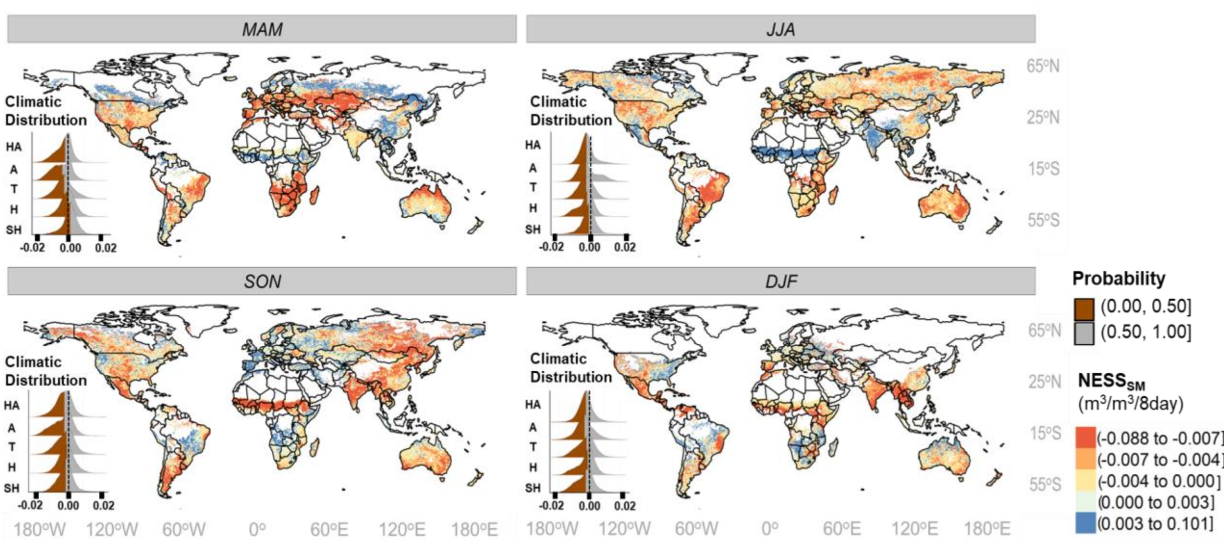

Figure 2. Global maps of Non-Equilibrium Steady State ($NESS_{SM}$) for four seasons - MAM, JJA, SON, and DJF. Insets show relative distribution of $NESS_{SM}$ amongst global hydroclimates (SH:

Super Humid, H: Humid, T: Temperate, A: Arid, HA: Hyper Arid). The vertical dashed line (black) in insets represent $NESS_{SM}$ of zero. The color sequential follows an approximate quantile division of data points. Missing/masked data are represented in white color.

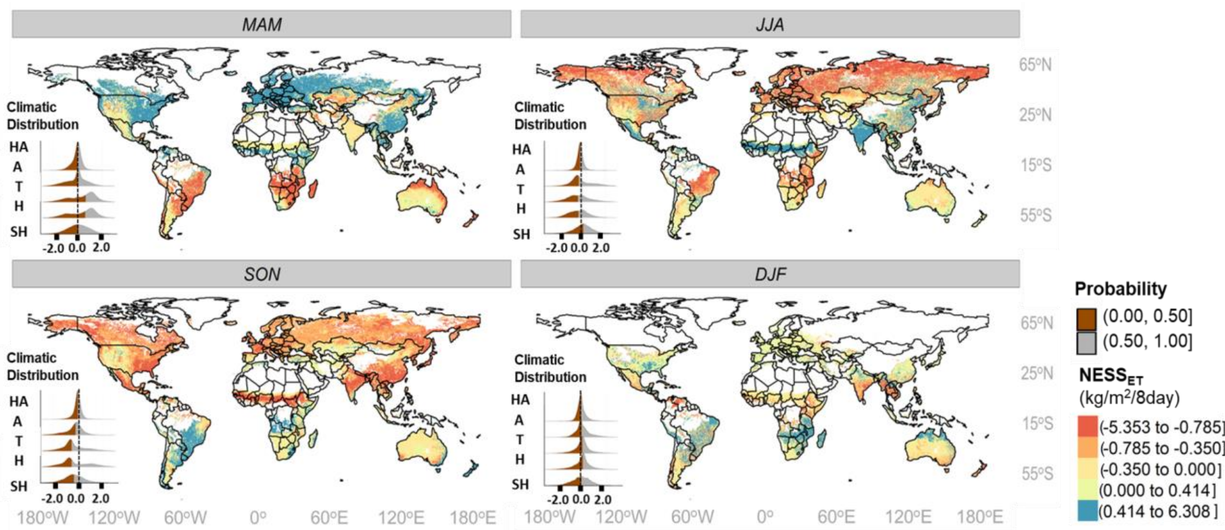

Figure 3. Global maps of Non-Equilibrium Steady State ($NESS_{ET}$) for four seasons - MAM, JJA, SON, and DJF. Insets show relative distribution of $NESS_{ET}$ amongst global hydroclimates (SH: Super Humid, H: Humid, T: Temperate, A: Arid, HA: Hyper Arid). The vertical dashed line (black) in insets represents $NESS_{ET}$ of zero. The color sequential follows an approximate quantile division of data points. Missing/masked data are represented in white color.

4.2 Global Wasserstein Distance (d_W) and the Coupling-Aridity Tradeoff

Fig. 4 showcases the seasonal variation in global d_W. A clear east-west division across CONUS is apparent in most seasons, however, the difference peaks during summer (JJA) and autumn (SON) months, albeit their causes remain divergent (explained through supplementary Fig. S1). Specifically, during JJA, eastern CONUS exhibits a fluctuating SM trailed by ET with land surfaces adjusting to the scattered patterns with the wet-delay enhancing as SON approaches.

Interestingly western CONUS exhibits lower d_W (i.e., immediate coupling) throughout summer (JJA) and autumn (SON) but the coupling shifts from preferentially dry to wet (insets in Fig. S1a). Similarly, the evergreen forests on the northwest corridor of CONUS showcase higher d_W which could be attributed to the lower impact of surface moisture on ET, indicating the resilience to hydrological droughts. A unique characteristic of continental climates such as Kazakhstan and Mongolia were the oscillating behavior between dry-coupled state in JJA to wet-coupled state in SON (insets in Fig. S1b). Such a strong oscillation could be attributed to the effect of hot winds from Iranian deserts during summer and the effect of cold air front from polar regions in winter, conjoined with meager oceanic influence. The insets provide histograms with wider variance in JJA as larger numbers of pixel values are available/retrieved. Interestingly, regions located at higher latitudes of North America, Europe and Asia displayed high d_W in JJA, however, we found a latitudinal partitioning (insets in Fig. S1a) existing between mid-northern latitudes (undergoing dry delay) and the northernmost corridor (undergoing a wet delay) preferably due to energy limited state.

The spatial heterogeneity witnessed across seasons was captured in coupling-aridity tradeoff (Fig. 4b) with temperate climates generally showing higher mean d_W (1.11 ± 0.25) while the coupling metric tapers out on either extreme (0.83 ± 0.15 for SH and 0.81 ± 0.18 for HA) (supplementary Table S3). This tradeoff bears implications on areas projected to witness stochastic changes in precipitation, and thereby, on atmospheric and soil aridity (Maestre et al., 2016). For instance, an increase in aridity would drag the SVA system into dry coupling state (lower d_W) making it vulnerable to atmospheric dryness (such as heat dome formation during sustained heat waves). Under such circumstances, surface moisture becomes crucial in guiding SM-ET coupling and frequent soil desiccation will significantly impact the microbial and organic load of topsoil

(Berdugo et al., 2020). Besides coupling, however, the resilience of SVA systems needs accounting for the absolute capacity of anomaly transference which necessitates changes in system's entropy production.

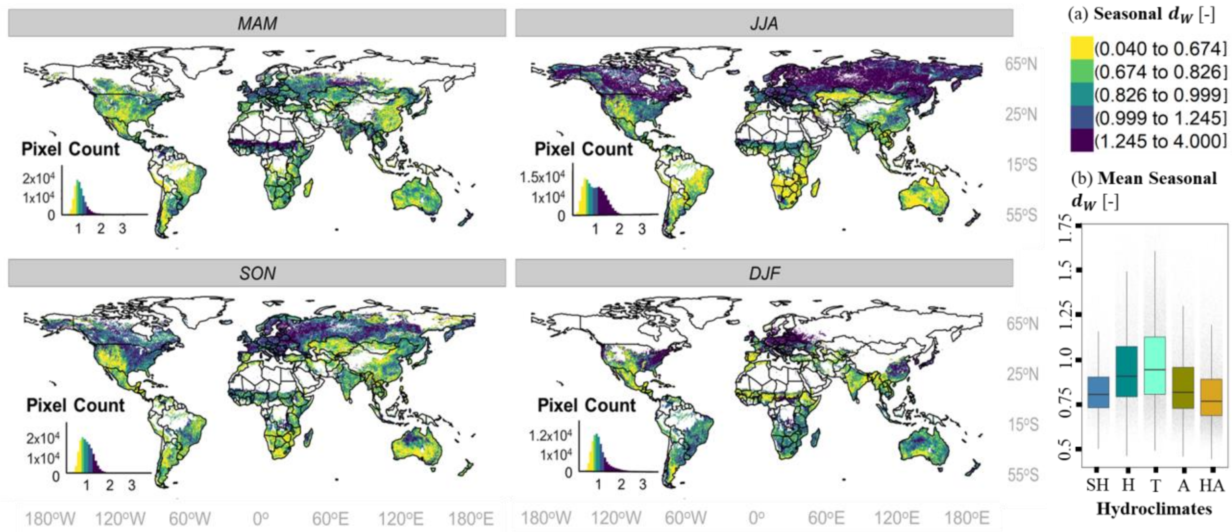

Figure 4. **(a)** Global maps of Wasserstein distance (d_W) signifying SM-ET coupling strength for four seasons - MAM, JJA, SON, and DJF. Insets show seasonal histogram of d_W. The color sequential follows a quantile division of data points. Missing/masked data are represented in white color. **(b)** Boxplots represent the global average distribution of d_W across hydroclimates (SH: Super Humid, H: Humid, T: Temperate, A: Arid, HA: Hyper Arid).

4.3 Complimentary evolution pathways for climatic regimes

During evolution, diverse paths of energy dispersal are explored in search of optimality (Feynman, 1948). This constrains the particles into obeying the entanglement ($\tau.\Delta\omega$) obtained from principle of least action that couples the flow of energy with time. The memory timescale τ is, hence, a natural outcome of entanglement with energy flowing down the potential gradient between the potential ω_{bl} at the atmospheric boundary layer and ω_{surf} at the land surface. These flows of energy propel systems towards more probable NESS eventually acquiring quasi-stationarity with respect to the surroundings (Tuisku et al., 2009).

Figure 5a shows the joint density plot for ${d_W}^2$ vs. $\Delta\omega$ matrix. The color gradient in grey scale reflects higher absolute values of slope factor γ. The dashed ellipses encompass the interquartile range of values for all the hydroclimates. The orientation of the climatic ellipses provides information about the relationship between the shifting dominant modes of evolution with changing aridity. The Eigenvectors associated with the major axis of the ellipse correspond to the dominant modes of evolution and characterizes the behavior of the system's state trajectory when subjected to the dynamics governed by the ${d_W}^2$ vs. $\Delta\omega$ matrix. For instance, the eigen vectors ($\overrightarrow{X_{SH}}$ & $\overrightarrow{X_{HA}}$) point towards the dominant direction of evolution for super humid (SH) and hyper arid (HA) climates. The arrows indicate the tendency of the systems to diminish the driving potential $\Delta\omega$. The approximate orthogonality between $\overrightarrow{X_{SH}}$ and $\overrightarrow{X_{HA}}$ suggests the complimentary evolutionary pathways adapted by either extremes for mitigating driving potential $\Delta\omega$. Physically, this symbolizes the scarcity of resources (water limitation in case of arid climates and energy limitation in case of humid climates) that generates this bias for the diverse pathway emergence as means of effective evolution. This is substantiated through the zoning of water surplus versus energy surplus systems (Fig. 5a) delineated by the minor axis of temperate ellipse extended throughout the space.

As evident from Fig. 5a, the system's state converges towards the global maxima for $|\gamma|$ over time, where γ value presents the sensitivity of SM-ET coupling to the driving force field. The convergence for all hydroclimates around this global maximum implicitly indicates the existence of optimal combination of coupling metric (${d_W}^2$) and driving force ($\Delta\omega$). The influence of different directions of the state-evolution is also suggestive of the fact that the cost paid by the hydroclimates in terms of memory timescale τ will be different. The global seasonal maps of relative time (τ/τ_0) is provided in the supplementary Fig. S4. Although there is significant heterogeneity in global values of (τ/τ_0), coherent regional patterns are also discernible. For instance, in United States with the advent of fall (SON) and winter (DJF) seasons, the atmospheric demand drops increasing τ/τ_0 for arid climates. Similarly, an increase in $\Delta\omega$ during spring (MAM) and summer months (JJA) reduces τ/τ_0 value in the higher latitudes. Furthermore, Fig. S2 and S3 represent inversely correlated spatial distributions in regions with negative γ and vice-versa.

Figure 5b substantiates the global maxima existence through the theoretical sensitivity plots for the relative time (τ/τ_0) as a function γ and $\Delta\omega$ for a unit $d_W{}^2$. τ/τ_0 indicates the deviation of actual memory timescale (τ) from inherent timescale (τ_0) of a pixel due to external driving forces. An increase in absolute value of γ leads to stable values for relative time $(\tau/\tau_0 \to 1)$, while a decreasing absolute value of γ leads to unstable values for relative time $(\tau/\tau_0 \to 0 \text{ or } \infty)$. A change in $\Delta\omega$ results in scaling of the τ/τ_0 without distorting the functional form. Figure 5c & 5d verifies this with variation seen in global hydroclimates for τ/τ_0 due to changes in $\Delta\omega$, i.e., the higher fluctuations of $\Delta\omega$ observed in arid climates creates extended diversions for the τ/τ_0, and the trend declines with increasing humidity.

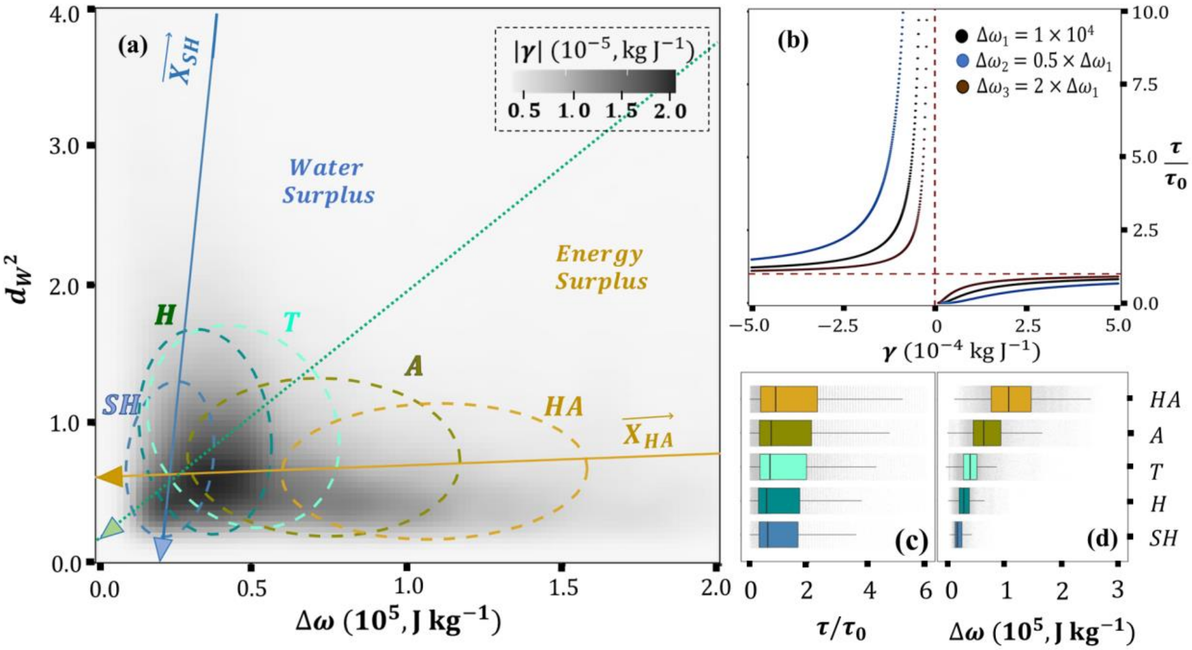

Figure 5. **(a)** The optimum zone of confluence (global maximum) for hydroclimates (SH: Super Humid, H: Humid, T: Temperate, A: Arid, HA: Hyper Arid) for $d_W{}^2$ vs. $\Delta\omega$ joint density plot with major Eigenvectors ($\overrightarrow{X_{SH}}$ & $\overrightarrow{X_{HA}}$) indicating differences in evolutionary pathways for superhumid (SH) and hyper arid (HA) climates. Dashed ellipses represent inter-quartile domain occupied by respective hydroclimates, while the inclined dotted line represents minor axis of temperate climate ellipse, corresponding to zoning of energy limited and water limited systems. The arrows on the eigen vectors indicate the tendency of systems to diminish the potential gradient to attain quasi-stationarity. **(b)** Sensitivity of τ/τ_0 to change in slope factor γ and potential gradient $\Delta\omega$ for a given coupling bound ($d_w{}^2 = 1.0$). **(c & d)** Hydroclimate wise boxplots for relative time (τ/τ_0) and potential gradient $\Delta\omega$. The observed variations in $\Delta\omega$ is reciprocated through variations in computed τ/τ_0.

4.4 Memory timescale and time-gradient entanglement

Typically, literatures suggest that the time taken by landscapes to dissipate an anomaly may range from ~ 10^3 secs (molecular diffusion scale) to ~ 10^7 secs (seasonal scale) (Ghannam et al., 2016; Haghighi et al., 2013; Wang et al., 2004; Wu & Dickinson, 2004). This spectrum in memory timescale spanning across 4 orders of magnitude is suggestive of the diverse mechanisms at interplay in SM-ET coupling. The global map of median τ (denoted as $\hat{\tau}$) across all seasons (MAM, JJA, SON, DJF) and its pdf is shown in Figure 6a (i) and (ii), while its seasonal map is provided in suppl. Fig. S4. The general observation in spatial median structure reflects a declining value of $\hat{\tau}$ with an increase in landscape aridity. This can be profoundly observed for arid and hyperarid regions across all major continents which stems from higher atmospheric demand, leading to quicker moisture depletion compared to temperate and humid climates. Interestingly, the pdf structure is positively skewed with dashed vertical lines representing 2 days (1^{st} quantile), 9 days (median) and 30 (3^{rd} quantile) days respectively. These values are in line with findings in earlier literatures that have reported timescales of 10.4 days for agricultural regions, < 20 days for grassland and > 30 days for regions with appreciable tree cover (Dardanelli et al., 2004; Teuling et al., 2006; McColl et al., 2017). The horizontal lines with arrows in Fig. 6a(ii) showcase the IQR spread of $\hat{\tau}$ observed for different hydroclimates, with a general trend of longer moisture dissipation timescale with increasing humidity.

Figure 6b showcases that the best fit for entanglement ($\tau. \Delta\omega$) optimization takes the functional form of exponential decay, parameterized using limit factor (α) and decay constant (λ). Two corollaries follow from this:

a) The rate of change $d\tau/d\Delta\omega$ is proportional to its current value τ, i.e., $d\tau/d\Delta\omega = -\lambda\tau$. Hence, the decay constant (λ) signifies the susceptibility of a system to change its response time (τ) for a unit shift in potential gradient.

b) When the potential gradient diminishes to zero, i.e., $\Delta\omega \rightarrow 0$, the anomaly timescale will tend to the limit factor, i.e., $\tau \rightarrow \alpha$.

The inset table in Fig. 6b provides median values for the α and λ for different hydroclimates and the ensemble (all hydroclimates taken together). Global estimates of these parameters can be crucial for predicting memory timescales for projected potential gradients in climate models (Koster & Suarez, 2001). The ensemble fit gives a good efficiency of Kling-Gupta Efficiency (KGE) of 0.54 with a decay rate of 1.10 x 10^{-5} Kg J^{-1} which is close to the temperate (T) climate with reasonably good efficiency (KGE = 0.47). However, on either extreme on aridity scale, λ value gets larger (with the exception for SH climate).

The faster decay of memory dissipation time for arid climates (Fig 6 (b)) can be ascribed to concomitant turbulent diffusivity whereby, the vapor transport in the top soil (~ 2 – 4 cm) is greatly enhanced by atmospheric turbulence (Brutsaert, 2014). This also suggests why a deterministic loss model works for arid conditions (McColl et al., 2019). On the other hand, larger λ values for humid climates can be attributed to the tendency of vegetation to lower their conductivity in order to evade cavitation (Katul et al., 2012; Manzoni et al., 2013). The incongruous behavior of SH model fit (KGE = - 0.34) is most likely due to significant observational uncertainties from SM and ET remote sensing and meteorological reanalysis data. Furthermore, the exponential decay model also implies the reasoning behind the emergence of coupling-aridity tradeoff, with the optimized product $(\tau.\Delta\omega)$ value higher for temperate climates relative to other climates. The non-linearity in time scale decay also signifies why usage of a linear correlation coefficient or variations thereof by prior studies (Koster et al., 2004; Seneviratne et al., 2010; Tuttle & Salvucci, 2016) might be a useful tool but can give contradictory results based on the run time considered for the analysis.

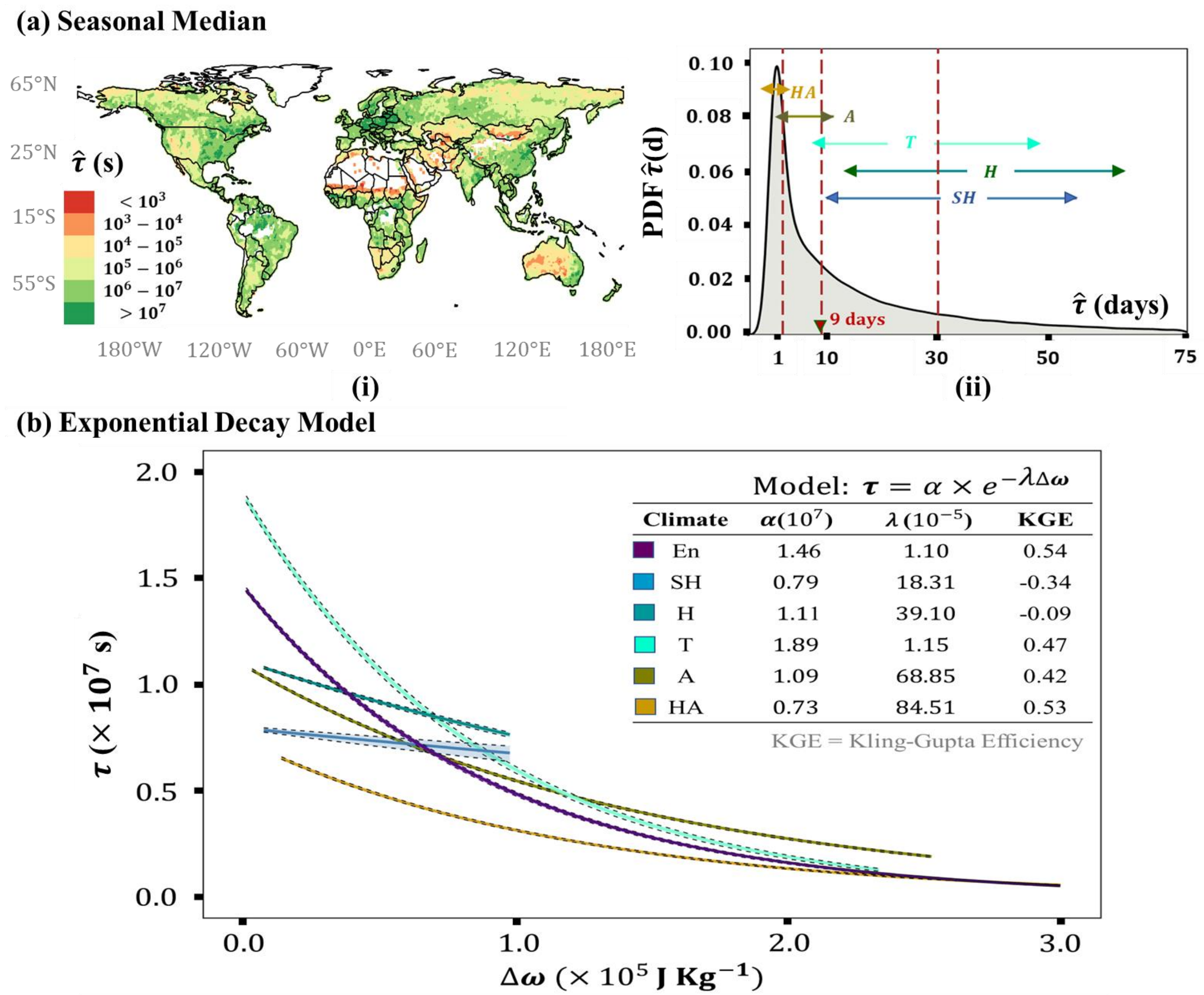

Figure 6. (a-i) Global map of median memory timescale ($\hat{\tau}$) across all seasons. **(a-ii)** Probability Density Function (pdf) of spatial distribution $\hat{\tau}$ values. The brown vertical dashed lines indicated 1st quartile, median, and 3rd quartile while horizontal bars show the IQR for different hydroclimates. **(b)** Memory timescale as a function of potential gradient follows an exponential decay model. Inset table quantifies the median values for fitted model parameters: α (limit factor) and λ (decay constant).

4.5 Lower Bound of Entropy Production and its seasonal variations

Although the concept of thermodynamics and entropy was first extensively introduced back in 1943 (Edlefsen & Anderson, 1943), the theoretical understanding of how entropy production is related to SM-ET coupling has been lacking. In practice, entropy production manifests itself in the form of dissipation (Kleidon, 2022) of energy that is irreversibly lost into the environment and hence, provides a quantitative characterization for investigating non-equilibrium processes. For seasonal Σ^* computation, we consider the entire tri-month period, i.e., τ = 90 days. Figure 7 shows that Σ^* varies greatly among regions, with predominant seasonal patterns in tandem with ET variability. Throughout all seasons, global arid and hyperarid regions produce lower amounts of entropy compared to vegetated and forested regions - primarily due to lower SM availability. This transcends to higher fluctuations prevalent in most parts of Europe, Russia, India, parts of Africa, and the northern borderline of Australia which mostly attribute to humid or temperate regions with stronger climatic influences. Both availability of moisture and energy drive entropy production, signifying the departure of the system from equilibrium conditions - $NESS_{SM}$ and $NESS_{ET}$ away from zero. Wet soil surfaces enhance the total heat flux from the surface into the boundary layer (Eltahir, 1998), thus producing higher entropy. Boxplots (Fig. 7b) suggest higher entropy production in super humid (24.30 ± 5.25 x10^{-6} J m^{-2} K^{-1}) and humid (21.10 ± 4.88 x10^{-6} J m^{-2} K^{-1}) regions and consistent decline in entropy with increase in aridity (suppl. Table S4). These findings are similar to a previous simulation study (Kleidon, 2008) which showcased that higher entropy is produced in regions with higher ET. However, the inclusion of d_W in our study differentiates systems based on their ability in utilization of available energy for unit anomaly transference. Thus, d_W can also be interpreted as an efficiency factor. This is critical to understand how the variability in SM-ET coupling will affect the ability of ecosystems to produce entropy which is a direct indicator of the capacity of the system to work.

Discrepancies in d_W hint to the fact that although entropy production is always positive, different ways of performing the same operation may incur more or less dissipation (Dechant &

Sakurai, 2019). Another conjecture from the coupling-aridity tradeoff and entropy production capacity is that for a given amount of flux and land temperature, temperate climates bear the least efficiency compared to other hydroclimates for unit anomaly transference. This could be argued to be most likely due to their bistable nature for soil moisture subsidence (Sehgal & Mohanty, 2023).

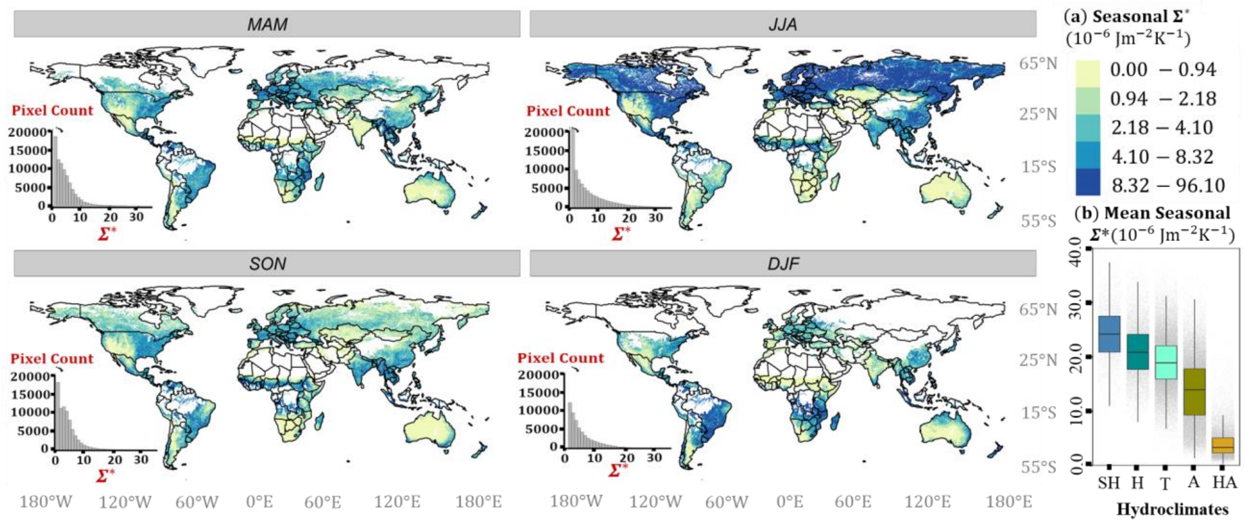

Figure 7. **(a)** Global maps of Entropy production (lower bound, Σ^*) for four seasons - MAM, JJA, SON, and DJF. Insets show seasonal histogram of Σ^*. The color sequential follows a quantile division of data points. Missing/masked data are represented in white color. **(b)** Boxplots represent the global average distribution of d_W across hydroclimates (SH: Super Humid, H: Humid, T: Temperate, A: Arid, HA: Hyper Arid).

4.6 Dissipative Energy Barriers for Terrestrial Ecosystems

Terrestrial biota substantially affects the exchange of fluxes rendering forests to be biologically the most productive ecosystem (Holdaway et al., 2010). However, maintenance of this productivity requires a continuous influx of solar energy and precipitation. Horowitz et al., (2017) argue that to maintain an arbitrary non-equilibrium state, a minimum rate of energy must be supplied and dissipated by the system. Hence, the influx of energy to ecosystems is accompanied by higher entropy production (or higher dissipation), implying a one-to-one correspondence between productivity and dissipative energy state the system is in. Therefore, there exists energetic barriers amongst ecosystems and by quantifying the amount of entropy production from SM-ET coupling, we can place terrestrial ecosystems in the context of dissipative energy states. Fig. 8a showcases global entropy thresholds for terrestrial ecosystems. Broadly, ecosystems display a hierarchy of entropy thresholds (i.e., e_1 through e_5) with increasing median energy dissipation levels from barren to forested ecosystems. Croplands are highly regularized systems and hence are considered as a reference case with respect to other systems which are subject to less human intervention. The difference in median energy levels represent the dissipative energy barriers (Δe) between ecosystems. The quantitative values are provided in supplementary Tables **S**5 and S6, while emphasis is laid on qualitative understanding in subsequent explanations.

One of the major imprints of climate change is projected to be global aridity shifts concurrently affecting multiple ecosystem functioning (Berdugo et al., 2020; Huang et al., 2016; Maestre et al., 2016). Earlier literatures have argued tropical forests and savannas to represent alternative stable states (Hirota et al., 2011), which align consecutively in the entropy hierarchy separated by an energy barrier Δe_{45}. Similarly, the lower we transcend in energy levels, the higher the dissipative energy barriers become between two ecosystems. For instance, the tipping of barren land ecosystems (with dissipative energy e_1) into forest ecosystems (with dissipative energy e_5) requires overcoming an energy barrier of Δe_{15} which is ~ 3 x Δe_{12} i.e., tipping of barren lands into grasslands. The lowest level of barren lands in entropy hierarchy is because of sparse vegetation cover (< 10% according to IGBP definition) and relatively infertile soil, while as the vegetation cover increases the dissipative capacity of the system improves. We argue that these energy barriers prevent ecosystems from undergoing catastrophic shifts (van Nes et al., 2016; Scheffer et al., 2001).

From the perspective of resilience, the ecosystem's response to perturbations could be understood as the entropy produced in adjusting to atmospheric conditions. Ecosystems with higher resilience will maintain their long-term seasonal behavior and gradually adapt or mitigate the effects of stochastic anomalies. We illustrate this by considering the Murray - Darling basin (MDB) in Australia for its diverse climate ranging from temperate in the south, subtropical in the north, to semi-arid in the west, and entails a variety of ecosystems (Fig. 8b). MDB has experienced a decline in rainfall, with area-average rainfall being lowest in the three years from Jan 2017 to Dec 2019 (Australian Bureau of Meteorology, 2020). Our results indicate that the resilience displayed to this dry period development, however, was different for different ecosystems (Fig. 8 c - e). Highest resilience was witnessed in forested ecosystems where changes in SM and Σ^* are asynchronous (Pearson r = -0.44) with Σ^* often lagging SM (Fig. 8c (i)). Furthermore, an insignificant cross-correlation factor (CCF) between d_W and Σ^* at 0 months lag (Fig. 8c (ii)) represents deviation of SM-ET coupling effect on Σ^*. On the contrary, for ecosystems with lower dissipative energy levels (i.e., Savannas and Grasslands), we observe an increasing synchrony (Pearson r = 0.35, 0.54) between SM and Σ^* (Fig. 8d-e (i)), most likely facilitated by increasing effect of surface SM-ET coupling (significant CCF at 0 months lag) on Σ^* (Fig. 8d-e (ii)). This is evident from a sustained negative SM and Σ^* anomaly throughout the dry period post 2017. In other words, such systems are vulnerable to climate anomalies and respond quickly (lower resilience). Hence, the results reflect upon two critical aspects (1) the variations in coping dynamics of systems subjected to prolonged state of perturbations are governed by dissipative energy levels at which the system can work, and (2) the tipping of a system will only be realized when the corresponding energy barriers are crossed frequently enough when supported by changes in aridity and energy influx.

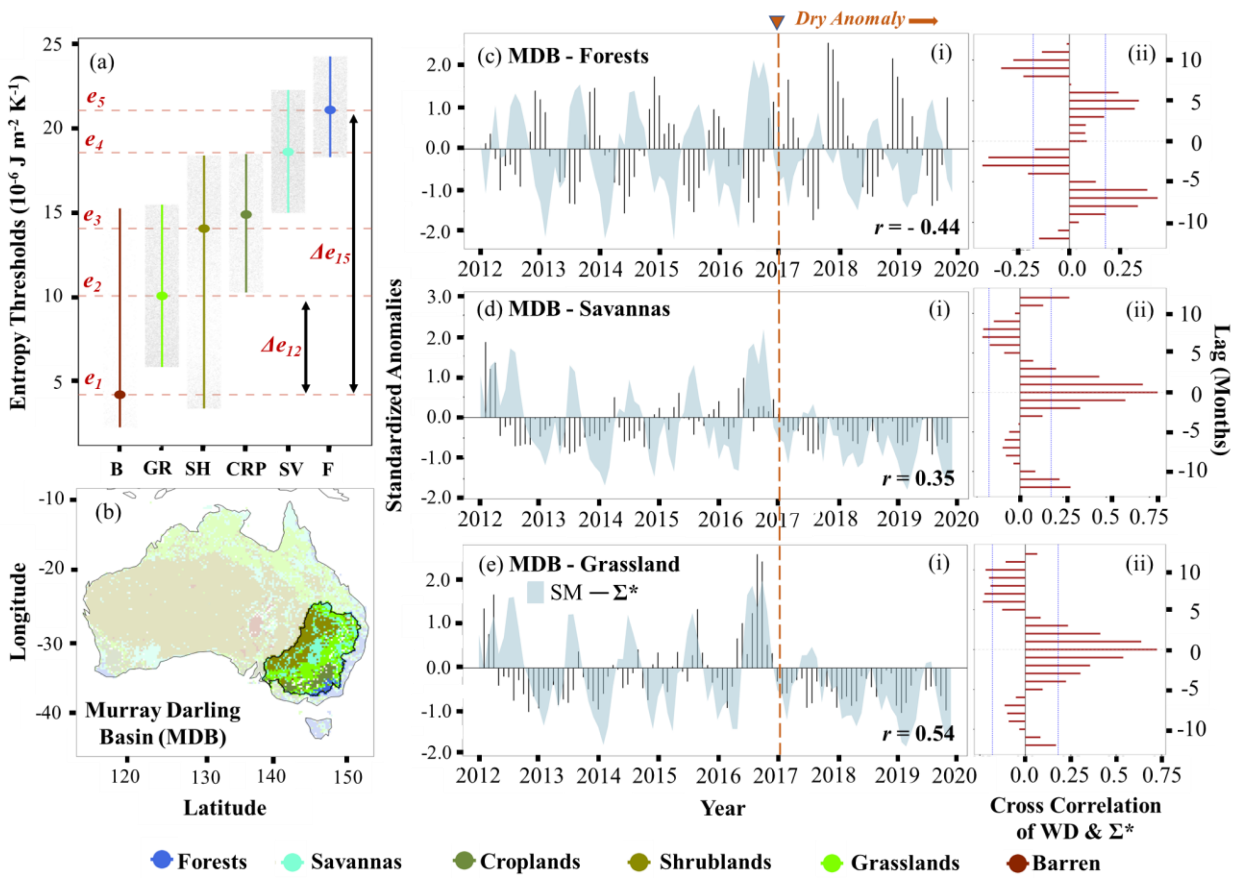

Figure 8. **(a)** Global entropic thresholds for different ecosystems (B: Barren, GR: Grassland, SH: Shrubland, CRP: Cropland, SV: Savanna, F: Forest). The length of vertical bars represents IQR and points represent the median Σ^* values. The horizontal lines (red, dashed) represent the median entropy values or dissipative energy levels (e_1, e_2, e_3, e_4, e_5), and the difference represents corresponding dissipative energy barriers (Δe). **(b)** Study area of Murray Darling Basin (MDB) in Australia. **(c-e) (i)** Time series plots of standardized anomalies of soil moisture (blue) and entropy production (black); the dashed line (orange) demarcates beginning of dry period in MDB, and **(ii)** Cross-correlation between mean monthly d_W and Σ^* computed for a lag of 12 months; the vertical blue lines represent 95% confidence interval.

5. Summary and Conclusion

This study provides a global assessment of entropic thresholds across various hydroclimates and their relationship with ecosystem resilience. Existence of water potential gradient (Δω) is utilized to formulate and define non-equilibrium steady states (NESS) as the state with nonzero fluxes and nonzero potential gradients (Qian, 2006) that hydroclimates hold-on to by dissipating energy to the environment. This dissipation physically manifests as entropy production when an imposed soil moisture (SM) anomaly is transferred to evapotranspiration (ET). For quantifying this SM-ET coupling and its relationship with entropy production, we introduce a new metric called the *Wasserstein distance* (d_W). The metric d_W is typically used in optimal transport (OT) discipline, and provides a measure of time evolution of probability density of a diffusing particle from one state to the other. Thus, d_W gives a new paradigm in deciphering system evolution through SM-ET coupling as water particle transitions in SVA continuum from soil to atmosphere. The global seasonal analysis for SM-ET coupling using remote sensing surface SM and ET data, establishes a "*coupling-aridity tradeoff*" with temperate climates operating at lower efficiencies per unit of flux and given surface temperature. This tradeoff bears greater implications on areas projected to witness aridity shifts in the future.

The optimization of SM-ET coupling transcends to $(\tau.\Delta\omega)$ entanglement, which is equivalent to *action* (per unit mass) in classical mechanics describing how a physical system evolves over time. Obeying *principle of least action* in the context of SM-ET coupling, ascertains that water particles follow the path that minimizes the time-averaged Δω. The memory timescale (τ) is, hence, a natural outcome of $(\tau.\Delta\omega)$ entanglement with energy flowing downhill. We apply this principle globally to compute τ which spans across four orders of magnitude, i.e., from molecular diffusion scale (~ 10^3 s) to seasonal scale (~ 10^7 s). The wider spectrum of timescales observed could be attributed to the scarcity of resources (water limitation versus energy limitation) that generates an evolutionary preference for hydroclimates. Through eigenvalue analysis, we prove the existence of such complementary evolution routes for major hydroclimates which are in search for an optimal combination of coupling metric (d_W) and driving potential ($\Delta\omega$). Such an optimum is possible when both physical and physiological controls on terrestrial water-energy coupling work on a "*similar strategy*" to mitigate atmospheric perturbations.

Extending the coupling formulation to compute lower bounds of entropy production (Σ^*), we observe that global arid and hyperarid regions produce less entropy compared to vegetated and forested regions - primarily due to lower SM availability. The major terrestrial ecosystems arrange themselves in a hierarchy of median entropic thresholds, with barren lands occupying the lowest level. The difference in these median entropic values represent the dissipative energy barriers (DEB) which prevents tipping of one ecosystem into another. The emergence of hierarchical DEB answers (1) why an inertia exists for systems to return to pre-anomaly conditions, and (2) if a tipping occurs, to which state the transition might happen! These findings are crucial for predicting how global ecosystems will respond to changing climate and for imposing effective constraints for simulating land-surface fluxes under a range of atmospheric forcings.

6. Acknowledgements

The authors acknowledge the funding support from NASA SMAP project (80NSSC20K1807). We thank the Texas A&M High-Performance Research Computing (HPRC) for providing computing resources for the research.

7. Open Research

C3S soil moisture is available at Copernicus climate data store (CCD): https://cds.climate.copernicus.eu/cdsapp#!/dataset/satellite-soil-moisture?tab=overview. Terra MODIS Net Evapotranspiration product (MOD16A2GF) is available at NASA LPDAAC: https://lpdaac.usgs.gov/products/mod16a2gfv006/. Bias-corrected near surface meteorological data is available at: https://cds.climate.copernicus.eu/cdsapp#!/dataset/derived-near-surface-meteorological-variables?tab=overview. Soil physical properties can be downloaded from: https://files.isric.org/soilgrids/latest/. Soil water characteristic parameters are available at: https://zenodo.org/record/6348799#.ZBn-y3bMKUn. Terra MODIS GPP product (MOD17A2H) is available at: https://lpdaac.usgs.gov/products/mod17a2hv006/, NDVI (MOD13A1) product is available at: https://lpdaac.usgs.gov/products/mod13a1v006/, and LAI product (MOD15A2H) is available at: https://lpdaac.usgs.gov/products/mod15a2hv006/. All MODIS data products were downloaded using Application for Extracting and Exploring Analysis Ready Samples (AρρEEARS). Global estimates of coupling metric (d_W), entropy bounds (Σ^*) and memory timescales (τ) can be found in supplemental material.

References

Annila, A., & Kuismanen, E. (2009). Natural hierarchy emerges from energy dispersal. *BioSystems*, *95*(3), 227–233. https://doi.org/10.1016/j.biosystems.2008.10.008

Benamou, J.-D., & Brenier, Y. (2000). A computational fluid mechanics solution to the Monge-Kantorovich mass transfer problem. *Numerische Mathematik*, *84*(3), 375–393. https://doi.org/10.1007/s002110050002

Berdugo, M., Delgado-Baquerizo, M., Soliveres, S., Hernández-Clemente, R., Zhao, Y., Gaitán, J. J., et al. (2020). Global ecosystem thresholds driven by aridity. *Science*, *367*(6479), 787–790. https://doi.org/10.1126/science.aay5958

Blöschl, G., & Sivapalan, M. (1995). Scale issues in hydrological modelling: A review. *Hydrological Processes*, *9*(3–4), 251–290. https://doi.org/10.1002/hyp.3360090305

Brutsaert, W. (2014). Daily evaporation from drying soil: Universal parameterization with similarity. *Water Resources Research*, *50*(4), 3206–3215. https://doi.org/10.1002/2013WR014872

Budyko, M. I. (1974). *Climate and life*. Academic press.

Crow, W. T., Berg, A. A., Cosh, M. H., Loew, A., Mohanty, B. P., Panciera, R., et al. (2012). Upscaling sparse ground-based soil moisture observations for the validation of coarse-resolution satellite soil moisture products. *Reviews of Geophysics*, *50*(2). https://doi.org/10.1029/2011RG000372

Dardanelli, J. L., Ritchie, J. T., Calmon, M., Andriani, J. M., & Collino, D. J. (2004). An empirical model for root water uptake. *Field Crops Research*, *87*(1), 59–71. https://doi.org/10.1016/j.fcr.2003.09.008

Dechant, A. (2022). Minimum entropy production, detailed balance and Wasserstein distance for continuous-time Markov processes. *Journal of Physics A: Mathematical and Theoretical*, *55*(9), 094001. https://doi.org/10.1088/1751-8121/ac4ac0

Dechant, A., & Sakurai, Y. (2019, December 18). Thermodynamic interpretation of Wasserstein distance. arXiv. https://doi.org/10.48550/arXiv.1912.08405

Dirmeyer, P. A. (2011). The terrestrial segment of soil moisture–climate coupling. *Geophysical Research Letters*, *38*(16). https://doi.org/10.1029/2011GL048268

D'Odorico, P., & Porporato, A. (2004). Preferential states in soil moisture and climate dynamics. *Proceedings of the National Academy of Sciences*, *101*(24), 8848–8851. https://doi.org/10.1073/pnas.0401428101

Dong, J., Akbar, R., Short Gianotti, D. J., Feldman, A. F., Crow, W. T., & Entekhabi, D. (2022). Can Surface Soil Moisture Information Identify Evapotranspiration Regime Transitions? *Geophysical Research Letters*, *49*(7), e2021GL097697. https://doi.org/10.1029/2021GL097697

Dosio, A., Mentaschi, L., Fischer, E. M., & Wyser, K. (2018). Extreme heat waves under 1.5 °C and 2 °C global warming. *Environmental Research Letters*, *13*(5), 054006. https://doi.org/10.1088/1748-9326/aab827

Edlefsen, N., & Anderson, A. (1943). Thermodynamics of soil moisture. *Hilgardia*, *15*(2), 31–298.

Eltahir, E. A. B. (1998). A Soil Moisture–Rainfall Feedback Mechanism: 1. Theory and observations. *Water Resources Research*, *34*(4), 765–776. https://doi.org/10.1029/97WR03499

Feldman, A. F., Short Gianotti, D. J., Trigo, I. F., Salvucci, G. D., & Entekhabi, D. (2022). Observed Landscape Responsiveness to Climate Forcing. *Water Resources Research*, *58*(1), e2021WR030316. https://doi.org/10.1029/2021WR030316

Feynman, R. P. (1948). Space-Time Approach to Non-Relativistic Quantum Mechanics. *Reviews of Modern Physics*, *20*(2), 367–387. https://doi.org/10.1103/RevModPhys.20.367

Fu, Z., Ciais, P., Feldman, A. F., Gentine, P., Makowski, D., Prentice, I. C., et al. (2022). Critical soil moisture thresholds of plant water stress in terrestrial ecosystems. *Science Advances*, *8*(44), eabq7827. https://doi.org/10.1126/sciadv.abq7827 van Genuchten, M. Th. (1980). A Closed-form Equation for Predicting the Hydraulic Conductivity of Unsaturated Soils. *Soil Science Society of America Journal*, *44*(5), 892–898. https://doi.org/10.2136/sssaj1980.03615995004400050002x

Ghannam, K., Nakai, T., Paschalis, A., Oishi, C. A., Kotani, A., Igarashi, Y., et al. (2016). Persistence and memory timescales in root-zone soil moisture dynamics. *Water Resources Research*, *52*(2), 1427–1445. https://doi.org/10.1002/2015WR017983

Grayson, R. B., Western, A. W., Chiew, F. H. S., & Blöschl, G. (1997). Preferred states in spatial soil moisture patterns: Local and nonlocal controls. *Water Resources Research*, *33*(12), 2897–2908. https://doi.org/10.1029/97WR02174

Gupta, S., Hengl, T., Lehmann, P., Bonetti, S., Papritz, A., & Or, D. (2020). Global soil saturated hydraulic conductivity map using random forest in a Covariate-based Geo Transfer Functions (CoGTF) framework at 1 km resolution [Data set]. Zenodo. https://doi.org/10.5281/zenodo.3934854

Gupta, S., Papritz, A., Lehmann, P., Hengl, T., Bonetti, S., & Or, D. (2022). Global maps of soil water characteristics parameters developed using the random forest in a Covariate-based GeoTransfer Functions (CoGTF) framework at 1 km resolution [Data set]. Zenodo. https://doi.org/10.5281/zenodo.6348799

Haghighi, E., Shahraeeni, E., Lehmann, P., & Or, D. (2013). Evaporation rates across a convective air boundary layer are dominated by diffusion. *Water Resources Research*, *49*(3), 1602–1610. https://doi.org/10.1002/wrcr.20166

Hirota, M., Holmgren, M., Van Nes, E. H., & Scheffer, M. (2011). Global Resilience of Tropical Forest and Savanna to Critical Transitions. *Science*, *334*(6053), 232–235. https://doi.org/10.1126/science.1210657

Holdaway, R. J., Sparrow, A. D., & Coomes, D. A. (2010). Trends in entropy production during ecosystem development in the Amazon Basin. *Philosophical Transactions of the Royal*

Society B: Biological Sciences, *365*(1545), 1437–1447. https://doi.org/10.1098/rstb.2009.0298

Horowitz, J. M., Zhou, K., & England, J. L. (2017). Minimum energetic cost to maintain a target nonequilibrium state. *Physical Review. E*, *95*(4–1), 042102. https://doi.org/10.1103/PhysRevE.95.042102

Huang, J., Yu, H., Guan, X., Wang, G., & Guo, R. (2016). Accelerated dryland expansion under climate change. *Nature Climate Change*, *6*(2), 166–171. https://doi.org/10.1038/nclimate2837

Kaila, V. R. I., & Annila, A. (2008). Natural selection for least action. *Proceedings of the Royal Society A: Mathematical, Physical and Engineering Sciences*, *464*(2099), 3055–3070. https://doi.org/10.1098/rspa.2008.0178

Katul, G. G., Oren, R., Manzoni, S., Higgins, C., & Parlange, M. B. (2012). Evapotranspiration: A process driving mass transport and energy exchange in the soil-plant-atmosphere-climate system. *Reviews of Geophysics*, *50*(3). https://doi.org/10.1029/2011RG000366

Kleidon, A. (2010). A basic introduction to the thermodynamics of the Earth system far from equilibrium and maximum entropy production. *Philosophical Transactions of the Royal Society B: Biological Sciences*, *365*(1545), 1303–1315. https://doi.org/10.1098/rstb.2009.0310

Kleidon, Axel. (2008). Entropy production by evapotranspiration and its geographic variation. *Soil and Water Research*, *3*(Special Issue 1), S89–S94. https://doi.org/10.17221/1192-SWR

Kleidon, Axel. (2022). Working at the limit: A review of thermodynamics and optimality of the Earth system. *Earth System Dynamics Discussions*, 1–46. https://doi.org/10.5194/esd-2022-38

Koster, R. D., & Suarez, M. J. (2001). Soil Moisture Memory in Climate Models. *Journal of Hydrometeorology*, *2*(6), 558–570. https://doi.org/10.1175/1525-7541(2001)002<0558:SMMICM>2.0.CO;2

Koster, R. D., Dirmeyer, P. A., & Guo, Z. (2004). Regions of Strong Coupling Between Soil Moisture and Precipitation. https://doi.org/10.1126/science.1100217

Lang, N., Jetz, W., Schindler, K., & Wegner, J. D. (2022, April 13). A high-resolution canopy height model of the Earth. arXiv. https://doi.org/10.48550/arXiv.2204.08322

Lehmann, P., Assouline, S., & Or, D. (2008). Characteristic lengths affecting evaporative drying of porous media. *Physical Review E*, *77*(5), 056309. https://doi.org/10.1103/PhysRevE.77.056309

Liu, Y., Holtzman, N. M., & Konings, A. G. (2021). Global ecosystem-scale plant hydraulic traits retrieved using model–data fusion. *Hydrology and Earth System Sciences*, *25*(5), 2399–2417. https://doi.org/10.5194/hess-25-2399-2021

Lopez, A. (2018). Soil moisture gridded data from 1978 to present [Data set]. ECMWF. https://doi.org/10.24381/CDS.D7782F18

Maestre, F. T., Eldridge, D. J., Soliveres, S., Kéfi, S., Delgado-Baquerizo, M., Bowker, M. A., et al. (2016). Structure and Functioning of Dryland Ecosystems in a Changing World. *Annual Review of Ecology, Evolution, and Systematics*, *47*(1), 215–237. https://doi.org/10.1146/annurev-ecolsys-121415-032311

Manzoni, S., Vico, G., Katul, G., Palmroth, S., Jackson, R. B., & Porporato, A. (2013). Hydraulic limits on maximum plant transpiration and the emergence of the safety–efficiency trade-off. *New Phytologist*, *198*(1), 169–178. https://doi.org/10.1111/nph.12126

McColl, K. A., Wang, W., Peng, B., Akbar, R., Short Gianotti, D. J., Lu, H., et al. (2017). Global characterization of surface soil moisture drydowns. *Geophysical Research Letters*, *44*(8), 3682–3690. https://doi.org/10.1002/2017GL072819

McColl, K. A., He, Q., Lu, H., & Entekhabi, D. (2019). Short-Term and Long-Term Surface Soil Moisture Memory Time Scales Are Spatially Anticorrelated at Global Scales. *Journal of Hydrometeorology*, *20*(6), 1165–1182. https://doi.org/10.1175/JHM-D-18-0141.1

McCurley Pisarello, K. L., & Jawitz, J. W. (2021). Coherence of global hydroclimate classification systems. *Hydrology and Earth System Sciences*, *25*(12), 6173–6183. https://doi.org/10.5194/hess-25-6173-2021

Mohanty, B. P. (2013). Soil Hydraulic Property Estimation Using Remote Sensing: A Review. *Vadose Zone Journal*, *12*(4), vzj2013.06.0100. https://doi.org/10.2136/vzj2013.06.0100

Nakazato, M., & Ito, S. (2021). Geometrical aspects of entropy production in stochastic thermodynamics based on Wasserstein distance. *Physical Review Research*, *3*. https://doi.org/10.1103/PhysRevResearch.3.043093

van Nes, E. H., Arani, B. M. S., Staal, A., van der Bolt, B., Flores, B. M., Bathiany, S., & Scheffer, M. (2016). What Do You Mean, ‘Tipping Point’? *Trends in Ecology & Evolution*, *31*(12), 902–904. https://doi.org/10.1016/j.tree.2016.09.011

Ouedraogo, F., Cherblanc, F., Naon, B., & Bénet, J.-C. (2013). Water transfer in soil at low water content. Is the local equilibrium assumption still appropriate? *Journal of Hydrology*, *492*, 117–127. https://doi.org/10.1016/j.jhydrol.2013.04.004

Perkins-Kirkpatrick, S. E., & Lewis, S. C. (2020). Increasing trends in regional heatwaves. *Nature Communications*, *11*(1), 3357. https://doi.org/10.1038/s41467-020-16970-7

Porada, P., Kleidon, A., & Schymanski, S. J. (2011). Entropy production of soil hydrological processes and its maximisation. *Earth System Dynamics*, *2*(2), 179–190. https://doi.org/10.5194/esd-2-179-2011

Qian, H. (2006). Open-System Nonequilibrium Steady State: Statistical Thermodynamics, Fluctuations, and Chemical Oscillations. *The Journal of Physical Chemistry B*, *110*(31), 15063–15074. https://doi.org/10.1021/jp061858z

Running, Steve, Mu, Qiaozhen, Zhao, Maosheng, & Moreno, Alvaro. (2019). MOD16A2GF MODIS/Terra Net Evapotranspiration Gap-Filled 8-Day L4 Global 500 m SIN Grid V006 [Data set]. NASA EOSDIS Land Processes DAAC. https://doi.org/10.5067/MODIS/MOD16A2GF.006

Scheffer, M., Carpenter, S., Foley, J. A., Folke, C., & Walker, B. (2001). Catastrophic shifts in ecosystems. *Nature*, *413*(6856), 591–596. https://doi.org/10.1038/35098000

Sehgal, V., & Mohanty, B. P. (2023). *Preferential Hydrologic States and Tipping Characteristics of Global Surface Soil Moisture* (preprint). Preprints. https://doi.org/10.22541/essoar.167840001.13313960/v1

Sehgal, V., Gaur, N., & Mohanty, B. P. (2021). Global Surface Soil Moisture Drydown Patterns. *Water Resources Research*, *57*(1), e2020WR027588. https://doi.org/10.1029/2020WR027588

Seneviratne, S. I., Lüthi, D., Litschi, M., & Schär, C. (2006). Land–atmosphere coupling and climate change in Europe. *Nature*, *443*(7108), 205–209. https://doi.org/10.1038/nature05095

Seneviratne, S. I., Corti, T., Davin, E. L., Hirschi, M., Jaeger, E. B., Lehner, I., et al. (2010). Investigating soil moisture–climate interactions in a changing climate: A review. *Earth-Science Reviews*, *99*(3), 125–161. https://doi.org/10.1016/j.earscirev.2010.02.004

Shokri, N., Lehmann, P., & Or, D. (2009). Critical evaluation of enhancement factors for vapor transport through unsaturated porous media. *Water Resources Research*, *45*(10). https://doi.org/10.1029/2009WR007769

Short Gianotti, D. J., Salvucci, G. D., Akbar, R., McColl, K. A., Cuenca, R., & Entekhabi, D. (2019). Landscape Water Storage and Subsurface Correlation From Satellite Surface Soil Moisture and Precipitation Observations. *Water Resources Research*, *55*(11), 9111–9132. https://doi.org/10.1029/2019WR025332

Structure and Interpretation of Classical Mechanics. (n.d.). Retrieved June 15, 2023, from http://groups.csail.mit.edu/mac/users/gjs/6946/sicm-html/

Sulla-Menashe, D., Gray, J. M., Abercrombie, S. P., & Friedl, M. A. (2019). Hierarchical mapping of annual global land cover 2001 to present: The MODIS Collection 6 Land Cover product. *Remote Sensing of Environment*, *222*, 183–194. https://doi.org/10.1016/j.rse.2018.12.013

Teuling, A. J., Seneviratne, S. I., Williams, C., & Troch, P. A. (2006). Observed timescales of evapotranspiration response to soil moisture. *Geophysical Research Letters*, *33*(23). https://doi.org/10.1029/2006GL028178

Tuisku, P., Pernu, T. K., Tuomas K. Pernu, Tuomas K. Pernu, & Annila, A. (2009). In the light of time. *Proceedings of The Royal Society A: Mathematical, Physical and Engineering Sciences*, *465*(2104), 1173–1198. https://doi.org/10.1098/rspa.2008.0494

Tuttle, S., & Salvucci, G. (2016). Empirical evidence of contrasting soil moisture–precipitation feedbacks across the United States. *Science*, *352*(6287), 825–828. https://doi.org/10.1126/science.aaa7185

Van Vu, T., & Saito, K. (2022, December 13). Thermodynamic Unification of Optimal Transport: Thermodynamic Uncertainty Relation, Minimum Dissipation, and Thermodynamic Speed Limits. arXiv. https://doi.org/10.48550/arXiv.2206.02684

Verbesselt, J., Umlauf, N., Hirota, M., Holmgren, M., Van Nes, E. H., Herold, M., et al. (2016). Remotely sensed resilience of tropical forests. *Nature Climate Change*, *6*(11), 1028–1031. https://doi.org/10.1038/nclimate3108

Vereecken, H., Kasteel, R., Vanderborght, J., & Harter, T. (2007). Upscaling Hydraulic Properties and Soil Water Flow Processes in Heterogeneous Soils: A Review. *Vadose Zone Journal*, *6*(1), 1–28. https://doi.org/10.2136/vzj2006.0055

Vereecken, Harry, Amelung, W., Bauke, S. L., Bogena, H., Brüggemann, N., Montzka, C., et al. (2022). Soil hydrology in the Earth system. *Nature Reviews Earth & Environment*, *3*(9), 573–587. https://doi.org/10.1038/s43017-022-00324-6

Wang, J., Salvucci, G. D., & Bras, R. L. (2004). An extremum principle of evaporation. *Water Resources Research*, *40*(9). https://doi.org/10.1029/2004WR003087

Wu, W., & Dickinson, R. E. (2004). Time Scales of Layered Soil Moisture Memory in the Context ofLand–Atmosphere Interaction. *Journal of Climate*, *17*(14), 2752–2764. https://doi.org/10.1175/1520-0442(2004)017<2752:TSOLSM>2.0.CO;2

Zhu, J., & Mohanty, B. P. (2002). Spatial Averaging of van Genuchten Hydraulic Parameters for Steady-State Flow in Heterogeneous Soils: A Numerical Study. *Vadose Zone Journal*, *1*(2), 261–272. https://doi.org/10.2136/vzj2002.2610

Supplementary Material

Thermodynamic Bounds of Terrestrial Water-Energy Coupling and Resiliency in Global Ecosystems

Debasish Mishra[1], Vinit Sehgal[1,2,3], Binayak Mohanty[1]*

[1]Biological and Agricultural Engineering, Texas A&M University, TX 77843, USA
[2]Water Management and Hydrological Science, Texas A&M University, TX 77843, USA
[3] Now at the School of Plant, Environment, and Soil Sciences, Louisiana State University, LA 70801, USA

*Corresponding author: Binayak P. Mohanty (bmohanty@tamu.edu)

Submitted to

Water Resources Research

Contents

Table S1. Signal to Noise ratio (SNR) blending period for the combined Copernicus Climate Change Service (C3S) soil moisture product.

Time Period	**Passive Sensors**	**Active Sensors**
2010-01-15 to 2011-10-04	AMSR-E, WindSat, SMOS	ASCAT-A
2011-10-05 to 2012-06-30	WindSat, SMOS	ASCAT-A
2012-07-01 to 2015-03-30	SMOS, AMSR2	ASCAT-A
2015-03-31 to 2015-07-20	SMOS, AMSR2, SMAP	ASCAT-A
2015-07-21 to 2020-12-31	SMOS, AMSR2, SMAP	ASCAT-A, ASCAT-B

Table S2. Description of surface meteorological (atmospheric), soil and vegetation variables used for quantification of dominant drivers controlling SM-ET coupling and entropy production.

Variable	Unit	Description
Near-surface air temperature (T_{air})	K	The temperature of air at 2 meters above the surface of land.
Near-surface specific humidity (q)	kg kg^{-1}	The amount of moisture in the air divided by the amount of air plus moisture at that location.
Near-surface wind speed (u_{surf})	m s^{-1}	The horizontal wind speed at a height of 10 meters above the surface of the Earth.
Surface air pressure (p_{atm})	Pa	The pressure (force per unit area) of the atmosphere at the surface of land.
Land Surface Temperature	K	Surface temperature of 0-5 cm depth soil profile.

Dry-Delayed vs Wet-delay Systems

These systems are supported by moisture influx from deeper horizons, necessitating the decoupling of surface moisture with subsurface moisture dynamics. Such coupling is most likely to prevail in mixed forests and native prairies. On the contrary, wet-delayed systems incorporate regions with delayed transfer of increased SM to an increase in ET. These regions are most likely energy limited and are typically found at higher latitudes such as the cold deserts of Siberia.

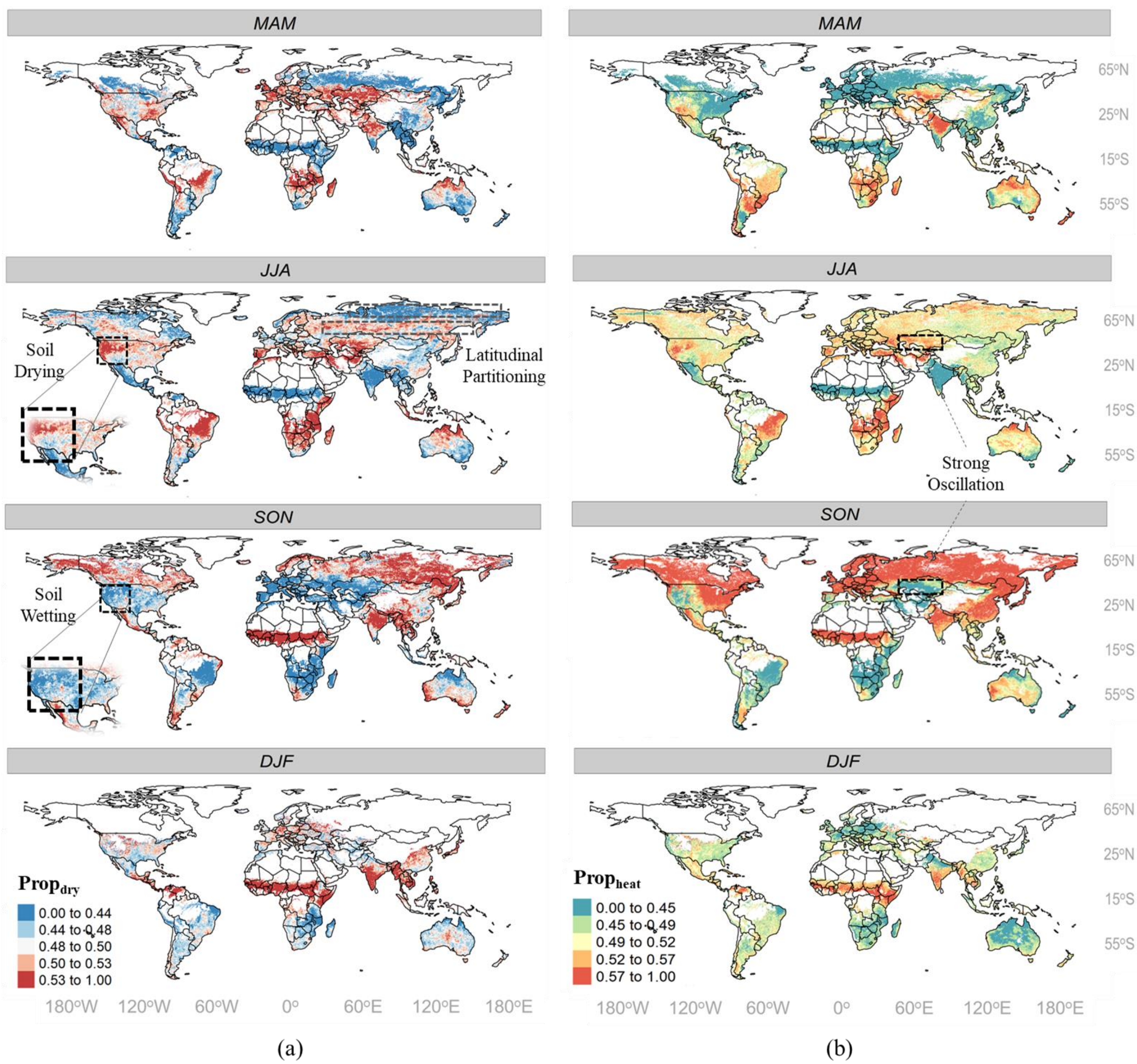

Figure S1. Global seasonal maps of **(a)** proportional duration spent by the pixel in SM drying ($SM_{AIF} < 0$) or SM wetting ($SM_{AIF} > 0$), and **(b)** proportional duration spent by the pixel in atmosphere heating ($ET_{AIF} < 0$) or cooling ($ET_{AIF} > 0$) for four seasons, namely, March through May—MAM, June through August—JJA, September through November—SON, and December through February—DJF. The color sequential follows a quantile division of data points. Missing/masked data are represented in white color.

Table S3. Statistical summary for seasonal Wasserstein distance, WD (-**)** across hydroclimates (IQR - Interquartile Range, SD - Standard Deviation, SE - Standard Error).

Climate	WD Median	WD IQR	WD Mean	WD SD	WD SE
Super Humid	0.806	0.172	0.834	0.147	0.002
Humid	0.993	0.351	1.017	0.229	0.002
Temperate	1.112	0.370	1.111	0.253	0.001
Arid	0.983	0.427	1.025	0.281	0.002
Hyper Arid	0.766	0.201	0.812	0.183	0.001

Seasonal Slope Factor (γ)

To compute the seasonal slope factor (γ), we compared two different methods – (a) quantile regression, (b) piecewise linear regression. Quantile regression divided the time series of a location based on four quantiles (i.e., 25th, 50th, 75th, 100th percentile) while piecewise regression discretized the data based into chunks of 3 months. However, the resulting raster's from both the methods did not have much difference, hence we selected piecewise linear regression for representing γ due to its conceptual proximity with the definition of "seasonality" (i.e., MAM, JJA, SON, DJF) used in the study.

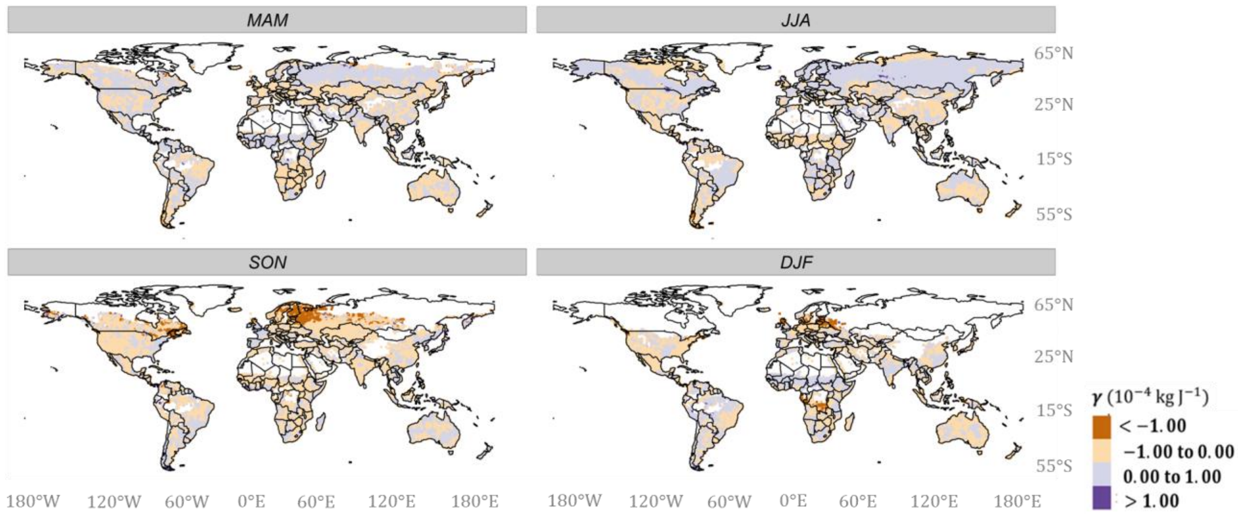

Figure S2. Global maps of seasonal slope factor, γ expressed in kg J^{-1} for four seasons, namely, March through May—MAM, June through August—JJA, September through November—SON, and December through February—DJF, computed using piecewise linear regression. Missing/masked data are represented in white color.

Relative time $(\boldsymbol{\tau/\tau_0})$

Due to discretization of γ, the resulting dimensionless quantity (τ/τ_0) might have few outliers which needs to be removed from further analysis. For example, if $\gamma \to 0$, $\tau/\tau_0 \to \infty$; such large outliers are impractical and were discarded from further analysis. Hence, values beyond 95th percentile were flagged out (i.e., values > 10000 were set equal to *NA*). Furthermore, it is important to note that as τ/τ_0 approaches zero (i.e., $\tau/\tau_0 \approx 0$ or $\tau_0 \gg \tau$), it physically represents the case where effective conductivity (K_{eff}) is very low or effective resistance (r_{eff}) is very high. This is visible (Fig. S3) in energy limited regions of Northern Eurasia and North America in the season of JJA, while regions with highest perturbations in atmospheric conditions, reflect the most variations in τ/τ_0.

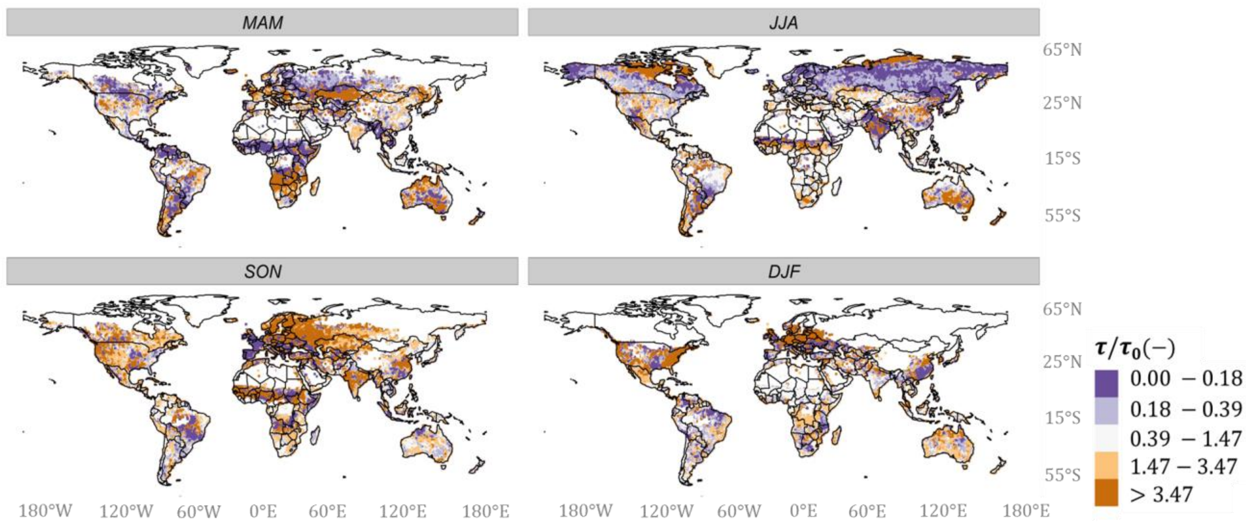

Figure S3. Global maps of relative time (τ/τ_0) for four seasons, namely, March through May—MAM, June through August—JJA, September through November—SON, and December through February—DJF. The color sequential follows a quantile division of data points. Missing/masked data are represented in white color.

Memory timescale ($\boldsymbol{\tau}$)

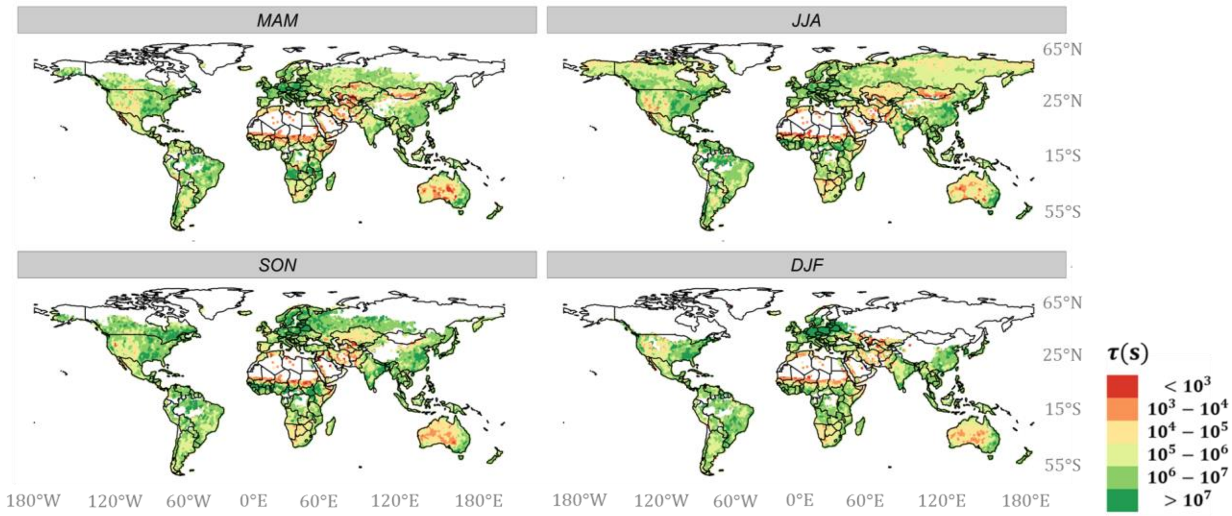

Figure S4. Global maps of memory timescale (τ), expressed in secs, for four seasons, namely, March through May—MAM, June through August—JJA, September through November—SON, and December through February—DJF. Missing/masked data are represented in white color.

Table S4. Statistical summary for seasonal entropy production, Σ* (10^{-6} J m^{-2} K^{-1}**)** across hydroclimates (IQR - Interquartile Range, SD - Standard Deviation, SE - Standard Error).

Climate	Σ* Median	Σ* IQR	Σ* Mean	Σ* SD	Σ* SE
Super Humid	24.200	6.670	24.300	5.250	0.0793
Humid	20.800	6.490	21.100	4.880	0.0422
Temperate	18.900	6.110	19.000	4.770	0.0212
Arid	14.000	8.530	13.800	5.680	0.0256
Hyper Arid	3.340	2.780	4.140	2.840	0.0186

Table S5. Statistical summary for seasonal entropy production, Σ* (10^{-6} J m^{-2} K^{-1}**)** across terrestrial ecosystems (IQR - Interquartile Range, SD - Standard Deviation, SE - Standard Error).

IGBP	Σ* Median	Σ* IQR	Σ* Mean	Σ* SD	Σ* SE
Forests	21.100	5.980	21.400	4.600	0.029
Savannas	18.600	7.280	18.300	6.440	0.031
Croplands	14.900	8.210	14.500	5.640	0.040
Shrublands	14.100	15.000	12.400	7.950	0.047
Grasslands	10.100	9.630	11.100	6.230	0.029
Barren	4.240	13.000	8.4500	7.750	0.195

Table S6. Dissipative energy barriers (Δe, 10^{-6} J m^{-2} K^{-1}) between terrestrial ecosystems computed as the difference between median entropy thresholds (Σ* Median from Table 5).

	Forests	**Savannas**	**Croplands**	**Shrublands**	**Grasslands**	**Barren**
Forests	0.000					
Savannas	2.400	0.000				
Croplands	6.200	3.700	0.000			
Shrublands	7.000	4.500	0.800	0.000		
Grasslands	11.000	8.500	4.800	4.000	0.000	
Barren	16.860	14.360	10.660	9.860	5.860	0.000